LJMU Research Online

Zaragoza-Cardiel, J, Beckman, JE, Font, J, García-Lorenzo, B, Camps-Fariña, A, Erroz-Ferrer, S, Barrera-Ballesteros, J, Cisternas, M, Fathi, K and James, PA

 Comparative internal kinematics of the H II regions in interacting and isolated galaxies: Implications for massive star formation modes

http://researchonline.ljmu.ac.uk/id/eprint/1829/

Article

For more information please contact researchonline@ljmu.ac.uk

Comparative internal kinematics of the H II regions in interacting and isolated galaxies: implications for massive star formation modes

Javier Zaragoza-Cardiel,[1,2]★ John E. Beckman,[1,2,3] Joan Font,[1,2]
Begoña García-Lorenzo,[1,2] Artemi Camps-Fariña,[1,2] Kambiz Fathi,[4] Philip A. James,[5]
Santiago Erroz-Ferrer,[1,2] Jorge Barrera-Ballesteros[1,2] and Mauricio Cisternas[1,2]

[1]*Instituto de Astrofísica de Canarias, C/ Vía Láctea s/n, E-38205 La Laguna, Tenerife, Spain*
[2]*Department of Astrophysics, University of La Laguna, E-38200 La Laguna, Tenerife, Spain*
[3]*CSIC, E-28006 Madrid, Spain*
[4]*Stockholm Observatory, Department of Astronomy, Stockholm University, AlbaNova, SE-106 91 Stockholm, Sweden*
[5]*Astrophysics Research Institute, Liverpool John Moores University, 146 Brownlow Hill, Liverpool L3 5RF, UK*

ABSTRACT

We have observed 12 interacting galaxy pairs using the Fabry–Perot interferometer GH αFaS (Galaxy H α Fabry–Perot system) on the 4.2-m William Herschel Telescope at the Observatorio del Roque de los Muchachos, La Palma. We present here the Hα surface brightness, velocity and velocity dispersion maps for the 10 systems we have not previously observed using this technique, as well as the physical properties (sizes, Hα luminosities and velocity dispersion) of 1259 H II regions from the full sample. We also derive the physical properties of 1054 H II regions in a sample of 28 isolated galaxies observed with the same instrument in order to compare the two populations of H II regions. We find a population of the brightest H II regions for which the scaling relations, for example the relation between the Hα luminosity and the radius, are clearly distinct from the relations for the regions of lower luminosity. The regions in this bright population are more frequent in the interacting galaxies. We find that the turbulence, and also the star formation rate (SFR), are enhanced in the H II regions in the interacting galaxies. We have also extracted the Hα equivalent widths for the H II regions of both samples, and we have found that the distribution of H II region ages coincides for the two samples of galaxies. We suggest that the SFR enhancement is brought about by gas flows induced by the interactions, which give rise to gravitationally bound gas clouds which grow further by accretion from the flowing gas, producing conditions favourable to star formation.

Key words: stars: formation – H II regions – galaxies: interactions – galaxies: ISM – galaxies: kinematics and dynamics.

1 INTRODUCTION

Galaxy mergers play an important role in galaxy evolution (White & Rees 1978), but it is still not clear whether, and if so how, they trigger star formation (Somerville et al. 2008; Bournaud 2011; Tadhunter et al. 2011), whether they stimulate nuclear activity (Canalizo et al. 2007; Bennert et al. 2008; Georgakakis et al. 2009; Cisternas et al. 2011; Ramos Almeida et al. 2011, 2012; Bessiere et al. 2012), and what are the mechanisms by which they produce new structures such as tails, bars and warps. They are important sites for the feedback processes, which are considered to be of considerable importance

in producing realistic galaxies in the context of Λ-cold-dark-matter cosmological models. (Bournaud et al. 2010; Hopkins et al. 2014)

Because mergers imply distortions quantifiable most accurately by kinematical studies of the galaxies as a whole, 3D studies of galaxy mergers are extremely important. Recently, Wisnioski et al. (2015) published a 3D study of galaxies with redshift $0.7 < z < 2.7$ claiming that the majority of galaxies are star forming and turbulent discs dominated by rotation and therefore not strongly affected by mergers. However, nearby galaxy studies can give us better clues in practical terms about how to study star-forming systems at higher redshifts, since we can achieve far better spatial resolution.

Star formation enhancement in galaxy collisions is theoretically well predicted for the central parts of the galaxies since collisions of galaxies tend to produce linear structures, inducing strong gas

★ E-mail: jzc@iac.es, javier.zaragoza@um.es

inflows towards the nucleus (Mihos & Hernquist 1996). However, the off-nuclear peaks of star formation, such as are clearly present in the Antennae galaxies, are much less well understood, and they are likely to be at least as important (Bournaud et al. 2010; Smith et al. 2014).

Hα emission is one of the most useful indicators of massive star formation in galaxies. Observing its full spectral profile is a very powerful tool for disentangling kinematics, but simply mapping the Hα surface brightness of a galaxy is already a comprehensive way to gain insight into global star formation. Kennicutt, Edgar & Hodge (1989), Bradley et al. (2006) studied the properties of the H II region populations, and in particular their luminosities, finding a break in the luminosity function at $\log L_{\text{H}\alpha} = 38.6$ dex, which some authors (Beckman et al. 2000) proposed could be used as a distance calibrator for galaxies. However, a physical basis for the break is desirable in order to strengthen its use as a distance calibrator, and while scenarios have been proposed (Beckman et al. 2000; Zaragoza-Cardiel et al. 2013), a clear explanation has not so far been agreed on.

Terlevich & Melnick (1981) studied the scaling relations of extragalactic H II regions measuring the sizes, luminosities, and velocity dispersions. They found that the luminosity, the size, and the velocity dispersion were correlated ($L \propto R^2$ and $L \propto \sigma_v^4$). The L–σ_v relation has also been proposed as a distance calibrator (Terlevich & Melnick 1981; Chávez et al. 2014). For this it is desirable to agree on a physical basis for the driver of the turbulence in H II regions, but there are a number of possible processes, which may combine in different proportions to produce the observed line widths. The studies by Terlevich & Melnick (1981), Zaragoza-Cardiel et al. (2013), Zaragoza-Cardiel et al. (2014) and Chávez et al. (2014) point towards self-gravity, at least in the more luminous regions, while Dyson (1979), Hippelein & Fried (1984), Rosa & Solf (1984) and Chu & Kennicutt (1994) favour supernova explosions and stellar winds. Gutiérrez, Beckman & Buenrostro (2011) used *HST* data from M51 to extract sizes and luminosities with unprecedented resolution and found similar scaling relations to those cited in the $L_{\text{H}\alpha}$–R relation.

However, our recent results (Zaragoza-Cardiel et al. 2013) found different scaling relations for the brightest set of H II regions in the interacting pair of galaxies Arp 270. We have found the same discrepancy in the H II regions of the Antennae galaxies (Zaragoza-Cardiel et al. 2014) who explain this as arising from two distinct populations of molecular clouds as they find an equivalent dichotomy in the molecular cloud population of the Antennae. This change in the scaling relations changes the behaviour of the star formation rate (SFR, derived from Hα luminosity) dependency on the parameters (mass, radius) of the star-forming regions.

Here we present new observations of 10 interacting galaxies with the Fabry–Perot interferometer GHαFaS (Galaxy Hα Fabry–Perot System). We have measured the basic physical parameters ($L_{\text{H}\alpha}$, R and σ_v) of each H II region and add equivalent data from the previous studies of interacting galaxies, Arp 270, and the Antennae galaxies, Zaragoza-Cardiel et al. (2013, 2014), respectively. We have extracted the same parameters for the H II regions of 28 isolated galaxies from Erroz-Ferrer et al. (2015) in order to compare results from the two samples.

For practical purposes we have called the galaxies which have no close neighbours and which therefore suffer negligible interaction with other galaxies 'isolated' even though the term is used in this article in a somewhat looser way than in studies dedicated to the careful definition of galaxies as isolated. The sample of isolated

galaxies was selected to spread the whole morphological types, and different absolute magnitudes ranging from -20.6 to -17.7.

In Section 2 we present the galaxy sample, the observations, and the data reduction. In Section 3 we present the moment maps of the interacting galaxies. In Section 4 we explain how we derive the parameters of the H II regions from those extracted directly from the observations. In Section 5 we present the physical properties of the H II regions in the interacting galaxies and in Section 6 those from the sample of isolated galaxies. In Section 7 we discuss the differences between the two samples, making comparison with previous studies, and in Section 8 we present a hypothesis to explain the zones of strong star formation well away from the galactic nuclei. Finally, in Section 9 we present our conclusions.

2 OBSERVATIONS AND GALAXY SAMPLE

We observed the interacting galaxies with GHαFaS (Hernandez et al. 2008), a Fabry–Perot interferometer mounted on the WHT (William Herschel Telescope) at the Roque de los Muchachos Observatory, La Palma. The optical colour composite images of the sample are in Fig. 1. The observations were taken during several observing runs between 2010 December and 2013 February (see Table 1).

These galaxies were selected from the catalogue of interacting galaxies by Arp (1966) and Vorontsov-Velyaminov, Noskova & Arkhipova (2001, except NGC 2146 and UGC 3995, which are classified as Galaxy pairs in de Vaucouleurs, de Vaucouleurs & Corwin 1976 and Karachentsev, Lebedev & Shcherbanovski 1985, respectively) according to the following criteria:

(i) Nearby systems ($V_{\text{sys}} < 10\,000$ km s^{-1}), in order to have adequate spatial resolution. From ~30 to ~ 100 pc in our sample.

(ii) Angular size which fits the GHαFaS field of view (FOV) and allows satisfactory sky subtraction.

(iii) Declination $-20° < \delta < 80°$, to ensure observations with air mass smaller than 1.6.

GHαFaS has a circular FOV of 3.4 arcmin diameter. The etalon has a free spectral range of 8 Å in Hα, which corresponds to a 390 km s^{-1} with a spectral resolution of 8 km s^{-1}. The pixel size is 0.2 arcsec, which gave us the values of seeing limited angular resolution given in Table 1. Further details about each galaxy observation are listed in Table 1. The morphological type, apparent and absolute magnitude of the whole sample of interacting galaxies are in Table 2. The comparison of these properties with those of the sample of isolated galaxies from Erroz-Ferrer et al. (2015), yields that both of them are spread over the whole morphological types, and that the interacting galaxies sample is brighter in average, although less than an order of magnitude. Thus, the galaxy masses (derived from absolute magnitude) in the interacting galaxies are higher in average compared to the masses in the isolated galaxies.

2.1 Data reduction

GHαFaS is mounted at the Nasmyth focus of the WHT without an optical derotator. Correction for field rotation is therefore necessary, and was performed using the technique described in detail in Blasco-Herrera et al. (2010). The observations are divided into individual cycles of 8 min, and each cycle is divided into 48 channels separated by 8 km s^{-1} and spanning the whole spectral range, which allows us to calibrate in velocity before applying digital derotation. We applied to the data cube for a given galaxy the procedures detailed in
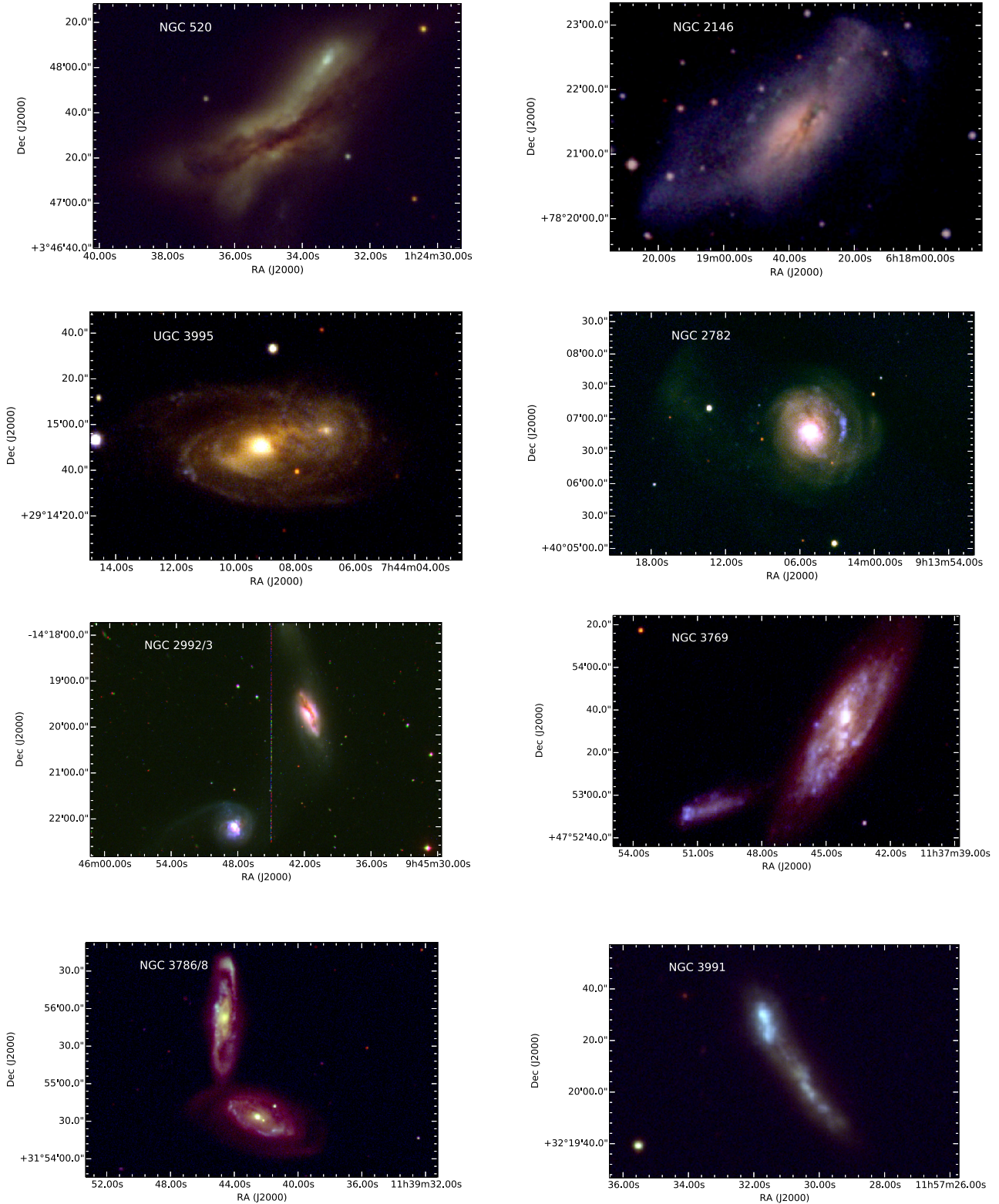
Figure 1. Colour composite images for the part of the sample of interacting galaxies; we present here new observations. All of them are combined using SDSS data, except NGC 2146 (using DSS), and NGC 2992/3 (using data from du Pont telescope at Las Campanas observatory).

Daigle et al. ([2006](#)), including phase-correction, spectral smoothing, sky subtraction and Gaussian spatial smoothing.

The flux calibration of the GHαFaS data cubes is performed using a continuum-subtracted and flux-calibrated ACAM (Auxiliary-port

CAMera, Benn, Dee & Agócs ([2008](#))) Hα image. ACAM is an instrument mounted permanently at the WHT used for broad-band and narrow-band imaging. We have followed the procedure explained in Erroz-Ferrer et al. ([2012](#)), which consists in measuring the flux

Table 1. Interacting galaxies observations log.

Name	RA (J2000) (hh:mm:ss)	Dec. (J2000) (° ′ ″)	Date (dd-mm-yyyy)	Exp time (min)	Seeing (arcsec)	Dist (Mpc)
NGC 520	01:24:35.1	+03:47:33	18-11-2012	181	0.9	34.4
NGC 2146	06:18:37.7	+78:21:25	23-12-2010	181	0.9	21.9
UGC 3995	07:44:09.3	+29:14:48	19-11-2012	181	1.0	60.6
NGC 2782	09:14:05.1	+40:06:49	17-11-2012	181	1.0	23.4
NGC 2992	09:45:42.0	−14:19:35	19-11-2012	156	1.0	31.6
NGC 2993	09:45:48.3	−14:22:06	18-11-2012	148	0.9	30.5
NGC 3769	11:37:44.1	+47:53:35	29-05-2011	156	0.8	16.1
NGC 3786	11:39:42.5	+31:54:33	28-02-2012	205	1.0	50.9
NGC 3788	11:39:44.6	+31:55:52	28-02-2012	205	1.0	50.1
NGC 3991	11:57:31.1	+32:20:16	04-02-2013	181	1.2	43.7

Table 2. Whole interacting galaxies sample. The apparent magnitude and the morphology are taken from Hyperleda (http://leda.univ-lyon1.fr; Paturel et al. 2003).

Name	m_B	M_B	Morphology
NGC 520	12.2	−20.48	Sa
NGC 2146	10.53	−21.17	SBab
UGC 3995	13.52	−20.39	Sbc
NGC 2782	12.32	−19.53	SABa
NGC 2992	13.06	−20.22	Sa
NGC 2993	13.11	−19.81	Sa
NGC 3395 (Arp 270)	12.4	−19.32	Sc
NGC 3396 (Arp 270)	12.43	−19.29	SBm
NGC 3769	12.54	−18.49	Sb
NGC 3786	13.47	−20.06	SABa
NGC 3788	13.44	−20.06	SABa
NGC 3991	13.51	−19.69	Im
NGC 4038 (Antennae)	10.85	−20.86	SBm
NGC 4039 (Antennae)	11.04	−20.67	SBm

from a set of selected H II regions in both the GHαFaS cube and the ACAM image, and calibrating by direct comparison.

3 MOMENT MAPS OF INTERACTING GALAXIES

For each galaxy data cube, we have extracted the Hα surface brightness, velocity and velocity dispersion maps using the tools described in Daigle et al. (2006). We show the maps in Fig. 2. The complete sample of the moment maps is available through CDS. We have also included in the information sent to CDS the continuum-subtracted Hα emission data cube.

4 PHYSICAL PROPERTIES OF H II REGIONS

We used ASTRODENDRO,[1] a PYTHON package to compute 'dendrograms' of astronomical data (Rosolowsky et al. 2008) to extract the relevant parameters of the H II regions from the data cubes. The parameters extracted are the Hα luminosity, $L_{H\alpha}$, the radius of the region, R, and the velocity dispersion, σ_v as explained in Rosolowsky & Leroy (2006) and Rosolowsky et al. (2008) from where we have extracted a brief description in order to make it easier to understand the present paper.

[1] http://www.dendrograms.org

We can describe a GHαFaS data cube as a collection of values, T_i, at a given point in the three dimensions which define the coordinates of the data cube, two spatial dimension, (x_i, y_i), and the third the velocity along the line of sight, v_i. The method considers that a region is separated from the rest of the cube by an isosurface of value T_{edge} where $T > T_{edge}$ inside the region and $T < T_{edge}$ just outside the region. The method then estimates the major and minor axes as the mean values of the second spatial moments in the directions of these axes, respectively;

$$\sigma_{maj,min} = \sqrt{\frac{\sum_i T_i (x_i - \bar{x})^2}{\sum_i T_i}}, \qquad (1)$$

where the sum is over the pixels inside the region, and x are the points lying on the major or the minor axes of the region.

The equivalent radius is then, $R = \eta \sqrt{\sigma_{maj} \sigma_{min}}$ where it is assumed that the region is spherical, so $\eta = 1.91$.

The second moment is used to estimate the velocity dispersion along the velocity axis weighted by the data cube values:

$$\sigma_v = \sqrt{\frac{\sum_i^{region} T_i (v_i - \bar{v})^2}{\sum_i^{region} T_i}}, \qquad (2)$$

where

$$\bar{v} = \frac{\sum_i^{region} T_i v_i}{\sum_i^{region} T_i}, \qquad (3)$$

and the sum is over all the pixels inside the region defined by T_{edge}. Equation (2) assumes that the observed Hα profiles are Gaussians. We plot a subsample of Hα profiles for a selection of the regions from our sample of galaxies observed with GHαFaS where we can check how Gaussian are the emission profiles in Fig. 3. We might expect to find multiple components in the emission profiles as well as broad wings typical of H II regions; however, the identification method differentiates between them if they are separated in the data cube by a few times the rms, and selects the Gaussian core. A more detailed study of multiple components and expansive superbubbles using GHαFaS observations is described in Camps-Fariña et al. (2015).

The zeroth moment is used to estimate the flux $F = \sum_i T_i \, \delta v \, \delta x \, \delta y$, where δx, δy, and δv are the pixel sizes.

A key reason to use this method is that it is unbiased with respect to T_{edge}. We adopt $T_{edge} = 4 \times l_{rms}$, set the intervals used in the process of searching for different H II regions to the same value as T_{edge}, and consider that the minimum area in pixels is the resolution of each observation. Three paradigms can be used with these method
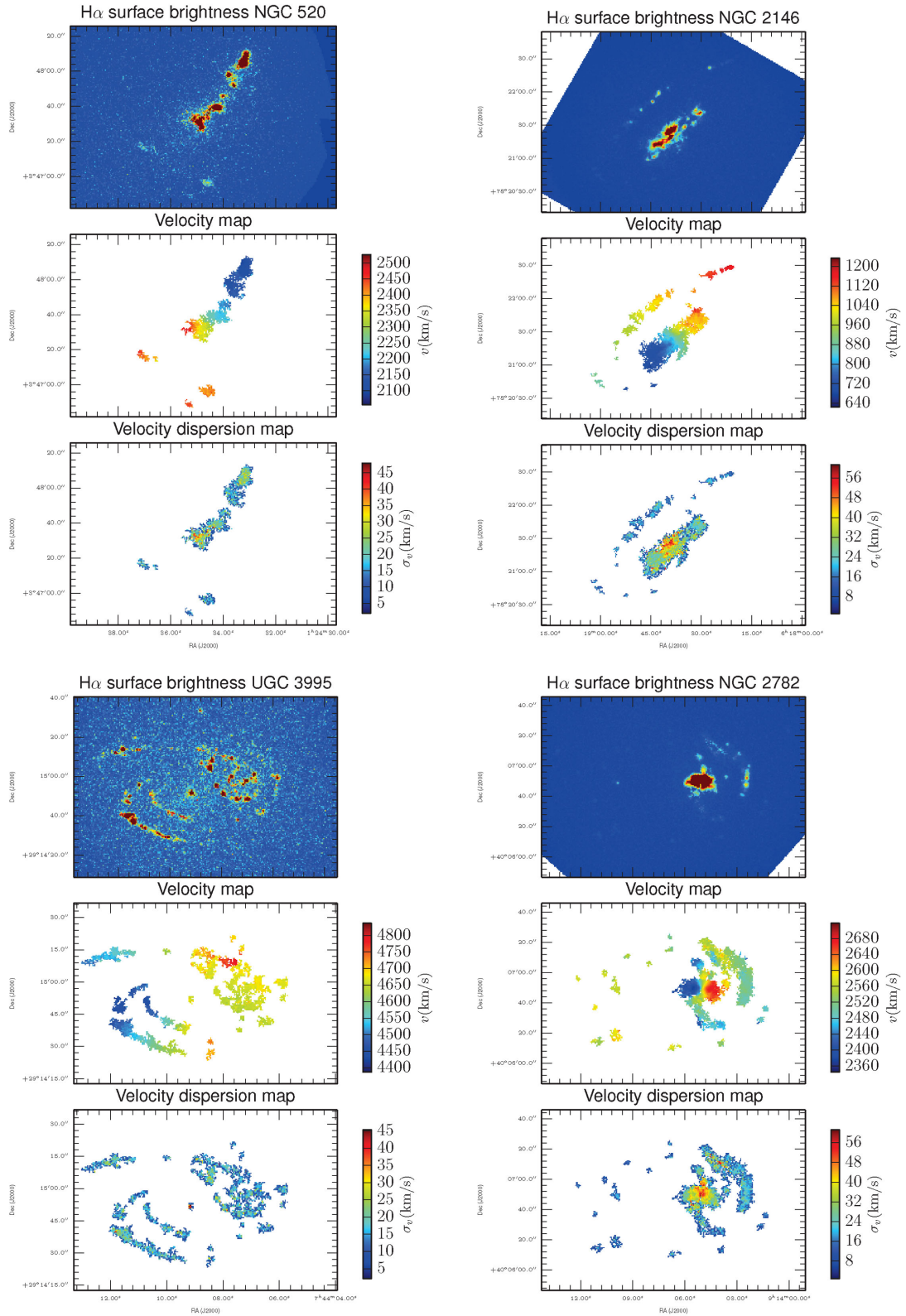
Figure 2. Moment maps of the interacting galaxies sample derived from the GHαFaS data cube. The moment maps are available through CDS.

described in Rosolowsky et al. (2008). We use here the 'bijection' paradigm.

Although correcting Hα for dust attenuation would strengthen our conclusions, making this correction would not affect the scaling relation behaviour, as we showed for the Antennae galaxies (Zaragoza-Cardiel et al. 2014) where there is quite heavy and variable dust attenuation (Brandl et al. 2005). In a very detailed study using *HST* Hα and continuum images of M51, Gutiérrez
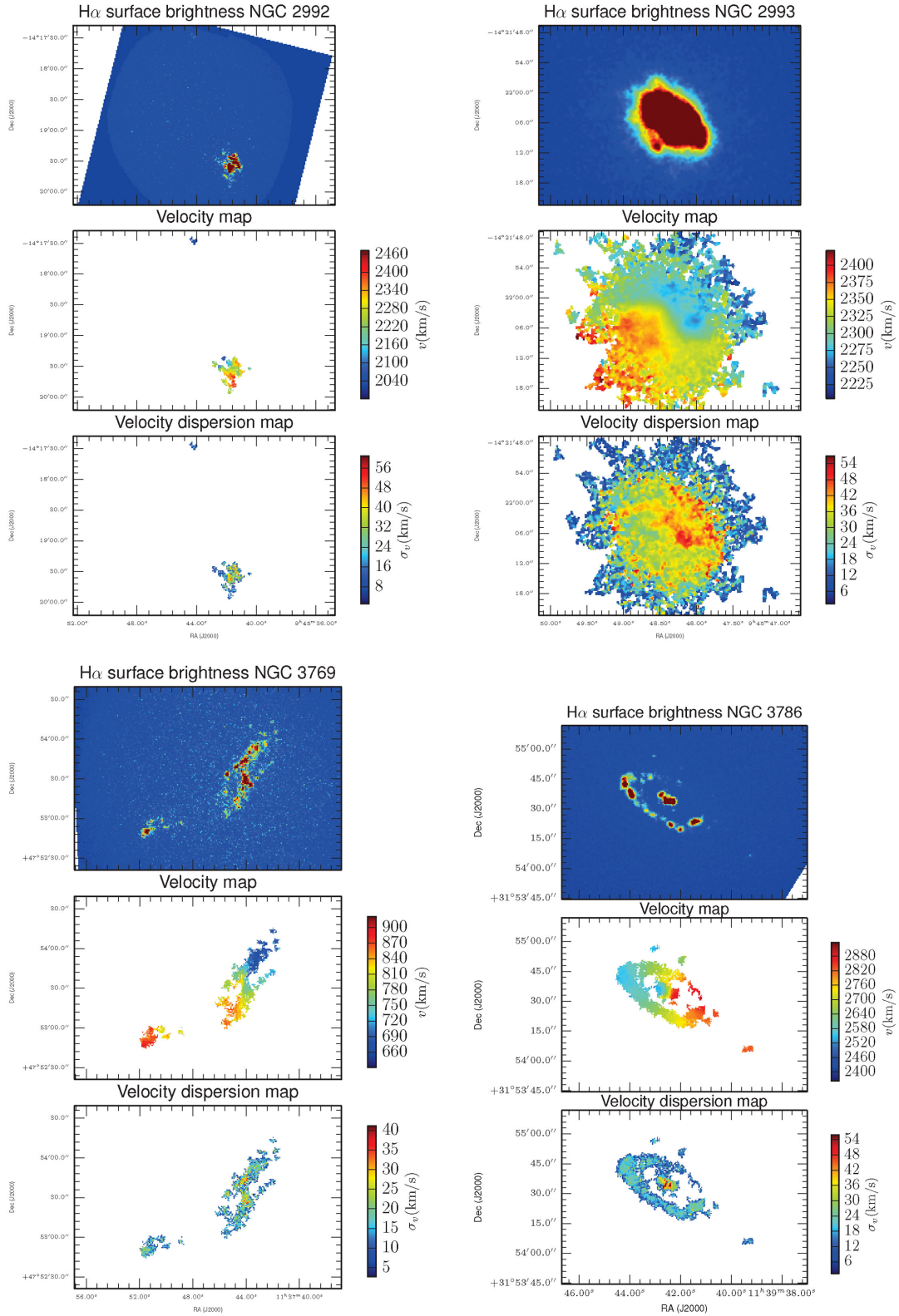
Figure 2. – *continued*

& Beckman (2010a) found that the dust attenuation is not a systematic function of H II region luminosity, or size. This is explained using an inhomogeneous model in which the bulk of the ionization occurs in denser clumps, in such a way that the dust attenuation depends on the mean clump size rather than on the overall size of the region. This implies that a statistical study of the type presented here should not be significantly affected.
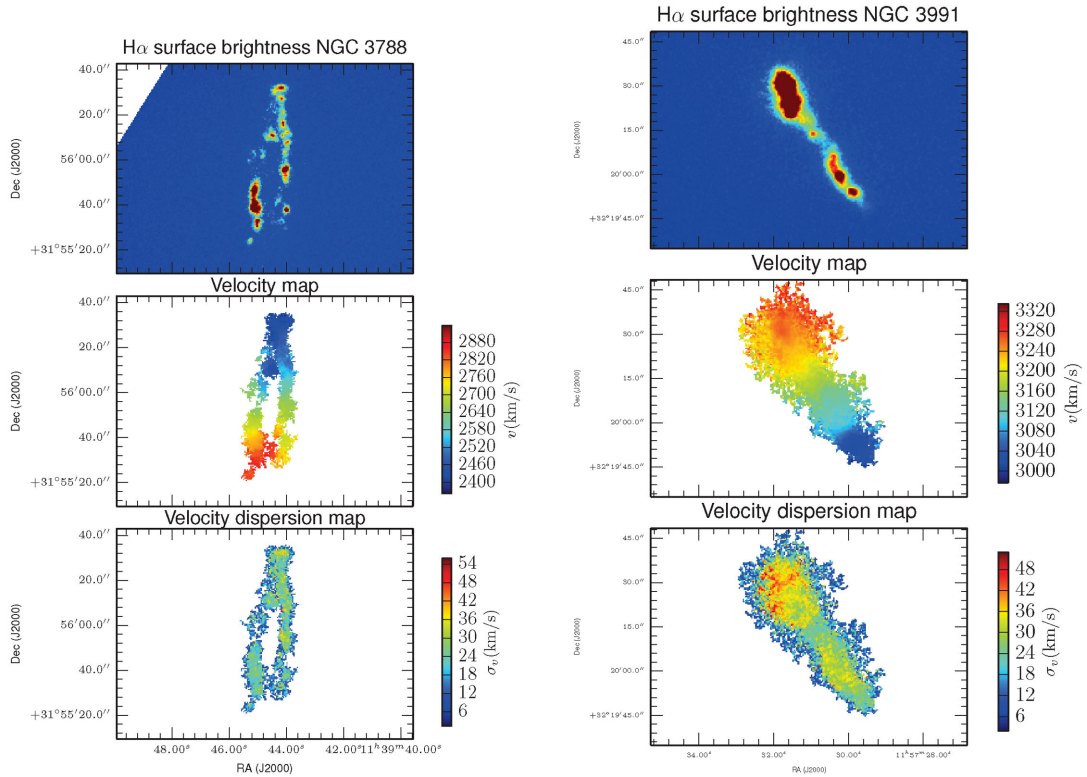
Figure 2. – *continued*

Given the Hα luminosity, $L_{H\alpha}$, and the size of the region, R, we can derive the mean electron density, n_e, following Relaño et al. (2005). Making a spherical first-order approximation for the H II regions (Spitzer 1978):

$$\frac{L_{H\alpha}}{\pi R_{cm}^2} = h\nu_{H\alpha}\alpha_{H\alpha}^{eff}(H_0, T)2.46 \times 10^{17} \times n_e^2 R_{cm}, \qquad (4)$$

where $h\nu_{H\alpha}$ is the energy of an Hα photon, $\alpha_{H\alpha}^{eff}(H_0, T)$ is the effective recombination coefficient of the Hα emission, and R_{cm} is the radius in cm. Equation (4) assumes no variation of the filling factor and of the ionizing photon scape probability with the properties of the regions. However, a comprehensive study of the filling factor for the H II regions in NGC 6946 by Cedrés et al. (2013) implies that there should be little variation in the effect of the filling factor on the mean electron density between larger and smaller H II regions, while a detailed study by Zurita et al. (2002) showed that the ionizing photon escape fraction does not show strong variations with luminosity (and size), as would be expected from regions with essentially clumpy structure (Giammanco et al. 2004).

Equation (4) also assumes that the source of ionization is only ionizing photons emitted by the massive stars, and does not include other sources of ionization such as shocks. Previous results reported in Calzetti et al. (2004) for a selection of galaxies suggest that the proportion of ionization by shocks is rather small compared to the effect of photoionization. The diagnostics used to disentangle the two possible contributions to the ionization are in any case degenerate, but previous work gives an upper limiting value of 33 per cent for the contribution due to the ionization by shocks, and a canonical value of 15 per cent (Hong et al. 2011).

From equation (4), we can derive the ionized gas mass, M_{HII}:

$$M_{HII}(M_\odot) = \frac{4}{3}\pi R^3 n_e m_p = 1.57 \times 10^{-17}\sqrt{L_{H\alpha} \times R^3}, \qquad (5)$$

where R is in pc, $L_{H\alpha}$ is in erg s^{-1}, and $m_p = 1.67 \times 10^{-27}$kg is the proton mass.

As in Terlevich & Melnick (1981), Blasco-Herrera et al. (2010), Zaragoza-Cardiel et al. (2013) and Zaragoza-Cardiel et al. (2014), the use of the velocity dispersion of the H II region gives us really new information about the physics in those regions when compared to previous purely morphological studies (Kennicutt et al. 1989; Bradley et al. 2006). We corrected the velocity dispersion for the instrumental, the natural ($\sigma_{v, n} = 3$ km s^{-1}), and the thermal ($\sigma_{v, th} = 9.1$ km s^{-1} line widths, assuming an isothermal H II region temperature of $T = 10^4$ K), and subtracting them in quadrature from the observed width. The instrumental velocity dispersion is derived from the neon calibration lamp using the emission line at 6598.9 Å. For each GHαFaS observation of one galaxy, a calibration data cube is taken, so we derive the instrumental velocity dispersion fitting a Gaussian to the brightest pixel of the calibration data cube (see Fig. 4). We only use as a valid velocity dispersions those with line widths greater than 8 km s^{-1}, i.e. velocity dispersions greater than 4 km s^{-1}, which is the effective velocity resolution of the instrument (8 km s^{-1} for GHαFaS).

We estimated the virial parameter, $\alpha_{vir} = 5\frac{\sigma_v^2 R}{GM_{gas}}$ (Bertoldi & McKee 1992), using the corrected velocity dispersion, the derived radius of the H II regions, and using the mass of the ionized gas as the gas mass, $M_{gas} = M_{HII}$ as a first approximation. The stellar mass inside H II regions is small (less than 4 per cent) compared with the total H II region mass (Relaño et al. 2005), so we use the size of the H II region and not that of the stellar ionizing cluster to

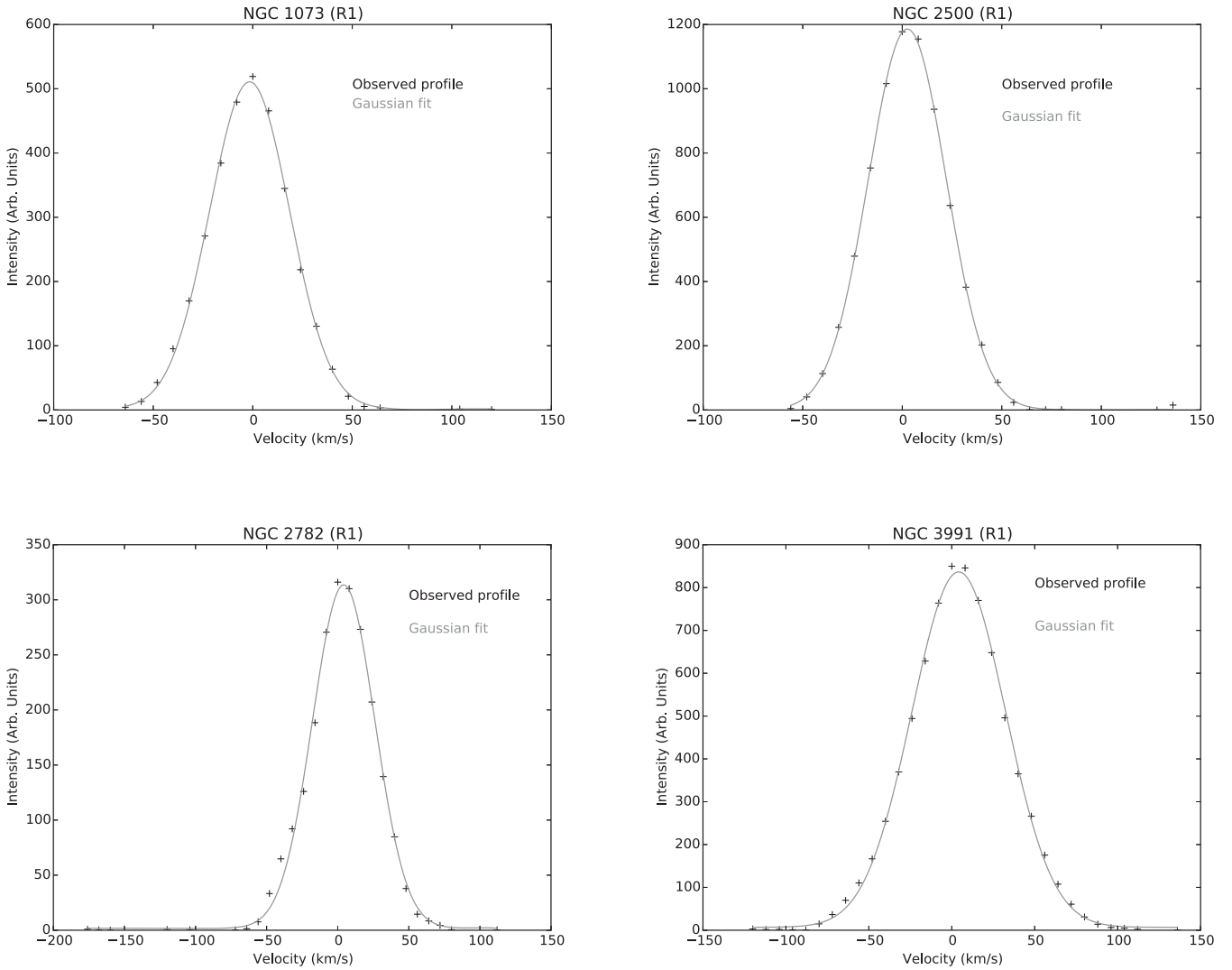**Figure 3.** Hα profile for a sample of the brightest H ɪɪ regions (region 1 in Tables A1 and A2) of a subsample of galaxies.
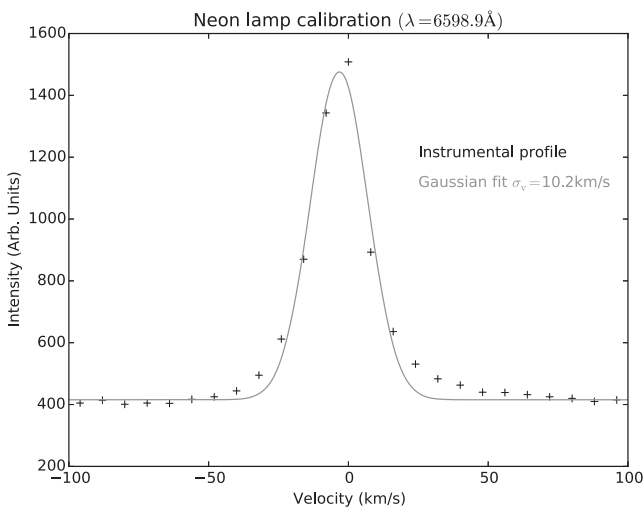

Figure 4. Emission profile of the neon calibration lamp at 6598.9 Å.

estimate the virial parameter. It is true that H ɪɪ regions, particularly large, luminous regions, have considerable neutral and molecular gas as well as ionized gas. In the larger more luminous regions, the ionized gas is an order of magnitude smaller than the neutral plus molecular gas (Yang et al. 1996; Giammanco et al. 2004). The results presented in Zaragoza-Cardiel et al. (2014) suggest that a constant ionization fraction is a good approximation, at least, for the correlations we are going to study here. Thus, the real virial parameters for all the regions will be a nearly constant fraction of those estimated here, between 0.05 (Zaragoza-Cardiel et al. 2014) and 0.1 (Yang et al. 1996; Giammanco et al. 2004), depending on the ionization fraction value. Since the virial parameter is in any case uncertain by a factor which depends in detail on the (non-uniform) density distribution and deviations from sphericity (Bertoldi & McKee 1992), the extra scatter in the uncertainty entailed by using ionized gas and a constant factor to make up the total gas mass will not seriously affect our results.

4.1 Uncertainties

We have estimated the uncertainties in the measured parameters following the bootstrapping method explained in Rosolowsky &

Leroy ([2006](#)). The method estimates the uncertainties by randomly sampling the values of the data cube for each region allowing repeated values, and then subtracts the parameter (luminosity, size or velocity dispersion) several times to estimate the standard deviation of these derived parameters. The uncertainty for each parameter is its standard deviation scaled up by the square root of the number of pixels in one resolution element. This uncertainty does not include the intrinsic error of the flux in the data cubes.

5 H II REGIONS IN THE INTERACTING GALAXIES

We present the parameters of the H II regions belonging to the interacting galaxies in Table A1. We have included the data for the interacting pair Arp 270 presented in Zaragoza-Cardiel et al. ([2013](#)), where we have reanalyzed the H II region parameters using ASTRO-DENDRO package in substitution of CLUMPFIND in order to produce a homogeneous study for the full set of galaxies. We present the reanalyzed H II regions of Arp 270 in Table A1. However, we have also used in the subsequent analysis the parameters of the H II regions of the Antennae galaxies presented in Zaragoza-Cardiel et al. ([2014](#)) in order to obtain a larger statistical sample of regions for the interacting galaxies. For these objects, we have 1259 H II regions in total. The parameter most sensitive to the noise level is the radius of the region, so in the following analysis we have removed the regions where the relative error in the radius is larger than 15 per cent. After applying this exclusion level we were left with 537 H II regions where the error in radius is sufficiently small, and for this sample the relative errors in the derived parameters – ionized gas mass, and electron density – are less than 20 per cent.

5.1 Scaling relations of H II regions

In Fig. [5](#) we plot the $L_{H\alpha}$–R relations for the H II regions for individual galaxies. We fit an x-axis error-weighted single linear fit, and also a double continuous x-axis error-weighted linear fit (four free parameters) using non-linear least squares to fit the double linear fit function to the data. We weight the error on the x-axis since the radii of the regions are the strongest source of uncertainty. We have chosen between a continuous double linear fit and a single one depending on the χ^2_{red} value, taking into account the addition of two free parameters more in the double linear fit. In the cases where χ^2_{red} is smaller for the double linear fit than in the single one, we choose the double continuous x-axis error-weighted linear fit:

$$\log(L_{H\alpha}) = L_1 + N_1 \log(R); \ \text{for} \ \log(R) < R_1$$
$$\log(L_{H\alpha}) = L_2 + N_2 \log(R); \ \text{for} \ \log(R) > R_1. \quad (6)$$

In the cases where χ^2_{red} is smaller for the single linear fit than in the double one, we choose the single linear fit $\log(L_{H\alpha}) = L_1 + N_1 \log(R)$. The results are in Table [3](#). For 8 of the 12 galaxies in the sample, we found a regime where the exponent N_1 and/or N_2 in the $L_{H\alpha}$–R relations is larger than 3. We have found that for the galaxies with a double linear fit, the exponent N_2 is larger than 3. Thus, the results for these larger (and brighter) H II regions are different, when compared to the results of Terlevich & Melnick ([1981](#)) and Gutiérrez & Beckman ([2010b](#)) for M51, where the maximum luminosity of its H II regions is not as high as for our sample of interacting galaxies, and similar to recent results of Zaragoza-Cardiel et al. ([2013](#), [2014](#)) for two of the systems included here, the Antennae and Arp 270. For two galaxies, NGC 2993 and NGC 3786, there are not enough fainter H II regions to perform a double linear fit, although they show an exponent in

the $L_{H\alpha}$–R relation also larger than 3, but we cannot separate them into two regimes. The Table [3](#) and the Fig. [5](#) are sorted by absolute magnitude, from brighter to fainter. The brightest regime where the exponent is larger than 3 is independent of the absolute magnitude.

An exponent larger than 3 in the $L_{H\alpha}$–R relation implies that the electron density (or the density of ionized gas) increases with the radius (and the luminosity) of the region. We show the n_e–R relation in Fig. [5](#) (below each $L_{H\alpha}$–R plot), where the electron density decreases with radius for the set of smaller (and fainter) H II regions for the interacting galaxies. In those cases we find a two-valued behaviour, density decreasing with radius in the small radius (i.e. low luminosity) part of the parameter space, and increasing with radius for large radii (i.e. large luminosities). This change is clearest for those systems with large numbers of luminous regions.

5.2 $L_{H\alpha}$–σ_v envelope

Since we have measurements of the velocity as a third dimension, we have used this to deepen our study of the H II regions. We plot the $L_{H\alpha}$–σ_v envelope in Fig. [6](#) (left) for all the H II regions from the sample of interacting galaxies. Relaño et al. ([2005](#)) suggested that the H II regions on the envelope are virialized in the sense that they are gravitationally dominated since those regions are the ones showing the minimum velocity dispersion for a given luminosity, and the excess for the regions away from the envelope can be attributed to internal motions which are not in quasi-equilibrium, such as recent contributions from stellar winds and supernovae. We have checked if the distance of an H II region, or a set of H II regions, from the envelope could be used as a parameter to distinguish between two density regimes. We estimated the envelope as described in Relaño et al. ([2005](#)), taking the H II region with the minimum velocity dispersion for each luminosity bin, and fitting a linear relation. The result is

$$\log(L_{H\alpha\,\mathrm{env}}) = 2.1 \times \log(\sigma_v) + 37.5, \quad (7)$$

where $L_{H\alpha\,\mathrm{env}}$ is in erg s^{-1} and σ_v is in km s^{-1}. We have divided the populations of H II regions, those which are on the envelope and obey $L_{H\alpha} > \frac{L_{H\alpha\,\mathrm{env}}}{40}$, and those which are not on the envelope and do not obey the previous inequality. This condition is plotted as a dashed line in Fig. [6](#) (left). We have plotted the electron density versus radius for all the H II regions from the sample of interacting galaxies in Fig. [6](#) (right). The two populations are clearly separated in the n_e–R relation plotted, where the grey points are for regions below the envelope, and the black points are on the envelope. The electron density decreases with the radius of the region for the regions below the envelope, and increases for the regions on the envelope, where the Hα luminosity depends superlinearly on the velocity dispersion (equation 7).

5.3 Virial parameter

We have estimated the virial parameter, $\alpha_{\mathrm{vir}} = 5 \frac{\sigma_v^2 R_{H\,\mathrm{II}}}{G M_{\mathrm{gas}}}$, which is the ratio between the kinetic and gravitational energy (Bertoldi & McKee [1992](#)), substituting the ionized gas mass, $M_{H\,\mathrm{II}}$, for the total gas mass, as a practical first approximation. The comparison between ionized and molecular gas in the Antennae galaxies (Zaragoza-Cardiel et al. [2014](#)) yields the result that the ionized gas mass must be a nearly constant fraction of the total gas mass. Since the virial parameter is affected by a further constant factor due to the density inhomogeneities and the non-sphericity of gas clouds, the use of the ionized gas mass yields a constant offset for the virial parameter. As we are making a comparative analysis of the two sets of H II
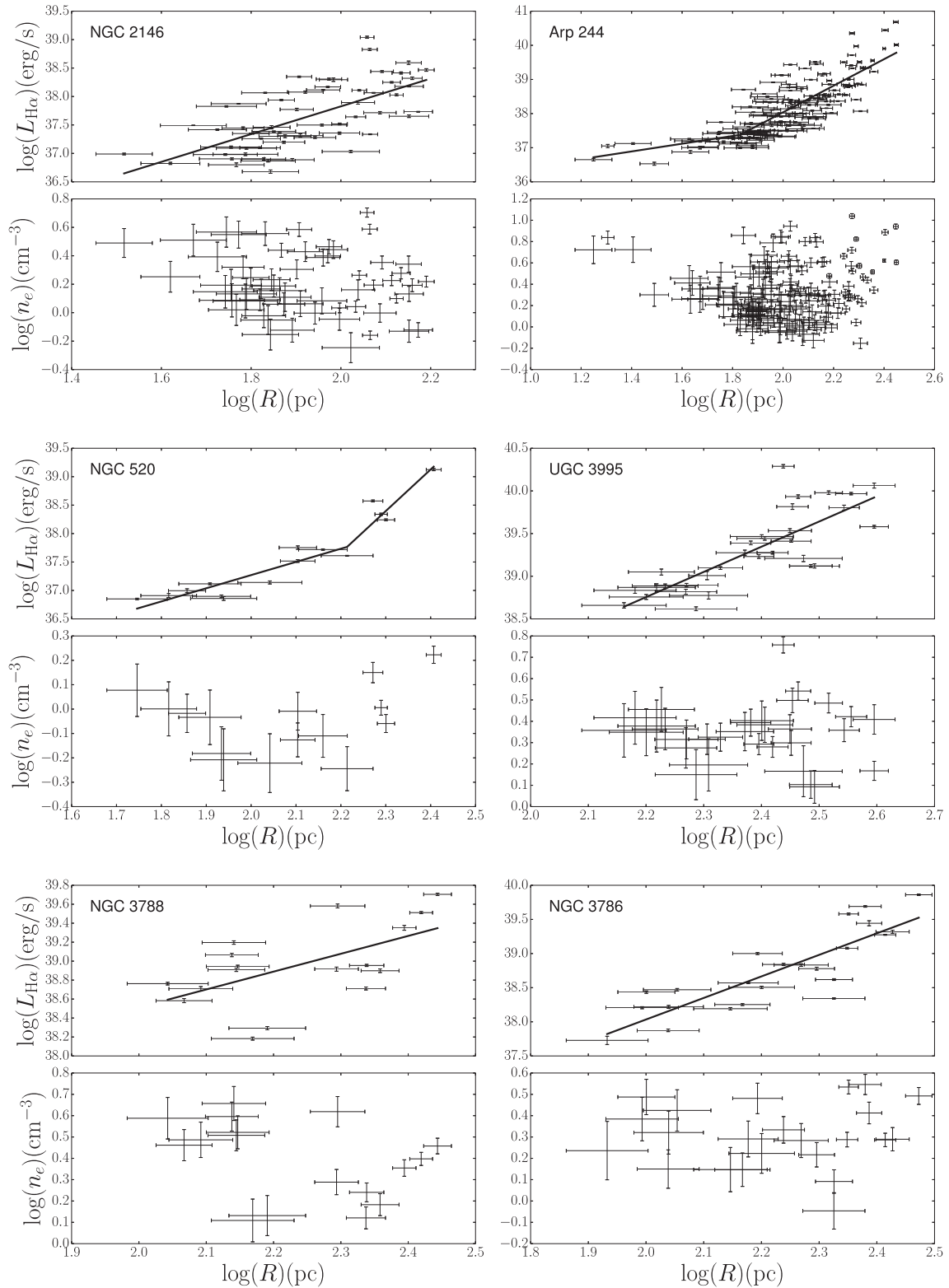
Figure 5. Hα luminosity, $L_{H\alpha}$, versus H II size (radius, R) for interacting galaxies. The result of the double (or single) linear fit is drawn as a solid line. The n_e versus R of H II regions in interacting galaxies is plotted below the $L_{H\alpha}$–R plot.

regions, we will neglect the numerical values of these offsets in the first instance.

We plot α_{vir} versus $L_{H\alpha}$ in Fig. 7 for all the H II regions together. We have used a result from the literature which shows that the H II

regions from the 'electron density decreasing' regime are pressure confined (Gutiérrez et al. 2011), and now we can check if the values of the virial parameter agree with this. $\alpha_{vir} \gg 1$ values, are for gas clumps confined by the external pressure. This explains why the
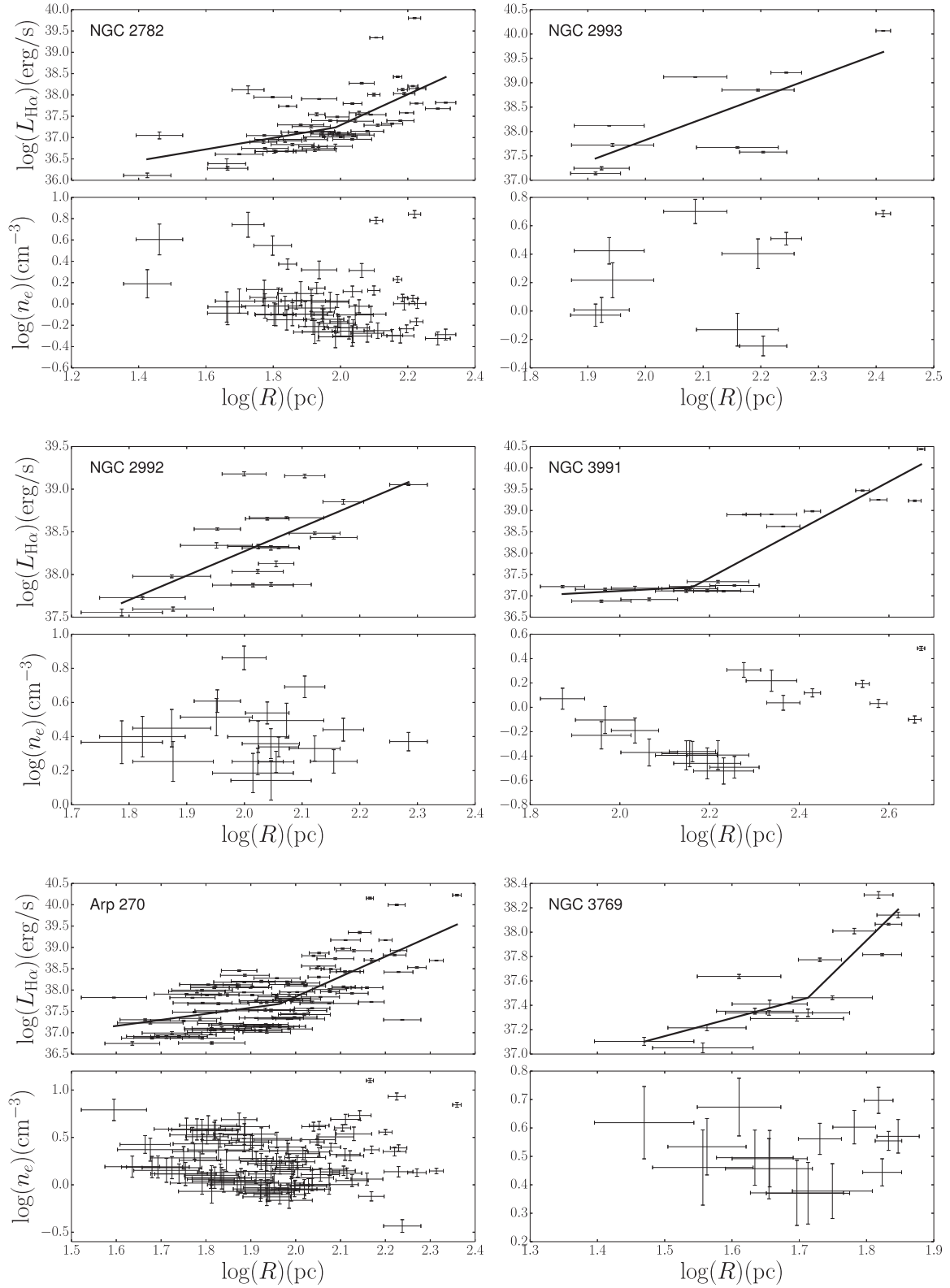
Figure 5. – *continued*

gas density decreases with size since the external pressure decreases with the distance from the galactic plane, with a scaleheight comparable with the sizes of the H II regions, so the bigger the region, the lower is the effective external pressure. Values of $\alpha_{\rm vir} \sim 1$ are for clouds where the self-gravity is the dominant force. The fact that the more massive clouds take values of this order implies that for clouds with masses sufficiently large the bigger the region, the stronger is the gravitational field so the density is an increasing function of radius. In Fig. 7 we can see that for the H II regions from the lower luminosity regime, the virial parameter lies in a range significantly

Table 3. Results of the single and double (when applicable) linear fits for interacting galaxies as defined in equation (6).

Name	N_1	L_1	N_2	L_2	$\log R_1$
NGC 2146	2.4	32.9			
Arp 244	1.1	35.3	3.8	30.2	1.8
NGC 520	2.3	32.6	7.3	21.5	2.2
UGC 3995	2.9	32.2			
NGC 3788	1.8	34.7			
NGC 3786	3.1	31.7			
NGC 2782	1.3	34.5	3.6	30.0	1.9
NGC 2993	4.3	29.0			
NGC 2992	2.8	32.5			
NGC 3991	0.5	35.9	5.6	25.0	2.1
Arp 270	1.4	34.8	4.7	28.4	1.9
NGC 3769	1.4	34.9	5.4	28.1	1.7

greater than unity, as predicted for pressure-confined H II regions. In contrast for the H II regions in the high-luminosity regime, the virial parameter lies close to a nearly constant value with mass, whose value is, apparently different from unity. However, if we take into account the results from Zaragoza-Cardiel et al. (2014) which give a nearly constant ionized gas fraction of ∼0.05, substituting the total gas mass for the ionized gas mass the virial parameter does lie close to unity, implying that the brightest H II regions are gravitationally bound.

6 H II REGIONS IN ISOLATED GALAXIES

We derived the parameters of the H II regions in isolated galaxies using observational data from the sample of 28 isolated galaxies in Erroz-Ferrer et al. (2015) observed with the same instrument, GHαFaS, and on the same telescope, WHT, as our sample of interacting galaxies. We present the parameters in Table A2 for 1054 H II regions. Again, we have used in the following analysis of H II regions in isolated galaxies, those regions with a fractional error in radius less than a 15 per cent since the radius of the regions is the most sensitive parameter. After applying this criterion we retained 1018 H II regions from the isolated galaxy sample.
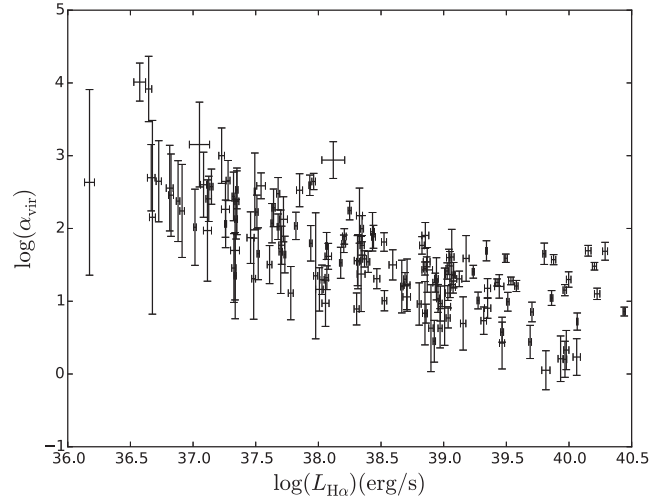

Figure 7. The virial parameter, $\alpha_{\mathrm{vir}} = 5\frac{\sigma_v^2 R_{\mathrm{HII}}}{G M_{\mathrm{gas}}}$ versus Hα luminosity, $L_{\mathrm{H}\alpha}$. We have used the mass of the ionized gas as the gas mass (in fact it should be a constant fraction of the total mass, but our qualitative conclusions do not depend on the value of this fraction, so we have not included it) $M_{\mathrm{gas}} = M_{\mathrm{HII}}$.

6.1 Scaling relations

We plot $L_{\mathrm{H}\alpha}$ versus R for the H II regions in isolated galaxies in Fig. 8.

Again, we have chosen between a continuous double linear fit or a single one depending on the χ^2_{red} value, taking into account the addition of two free parameters more in the double linear fit. The results of the linear fits are in Table 4. We find an exponent N_1 and/or N_2 larger than 3 in the $L_{\mathrm{H}\alpha}$–R relation in only 6 of the 28 isolated galaxies. Thus, the regime where the ionized gas density increases with size (and luminosity) in the isolated galaxies is much less frequent than in the interacting galaxies.

In Fig. 8 (below each $L_{\mathrm{H}\alpha}$–R relation) we plot the electron density versus the radius of the H II regions for each individual galaxy. For the regions in the isolated galaxies we find in some cases a regime where the electron density increases with radius but where this occurs there are relatively few H II regions and the phenomenon is
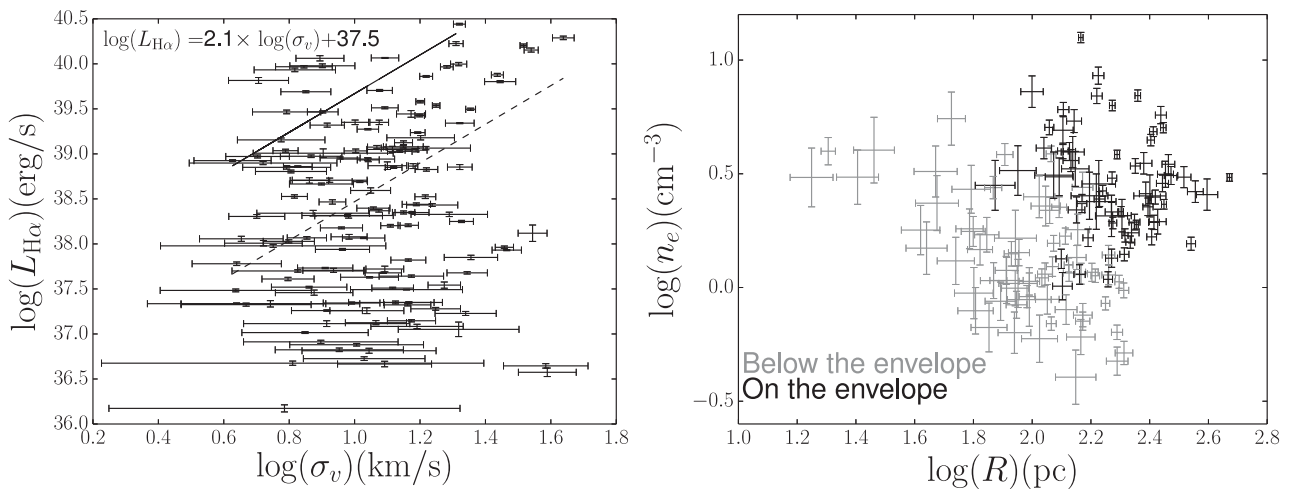
Figure 6. Left: Hα luminosity, $L_{\mathrm{H}\alpha}$, versus velocity dispersion, σ_v, for H II regions in interacting galaxies. We have plotted the fitted envelope as a solid line, and the displaced envelope condition explained in the paper, as a dashed line. Right: electron density, n_{e}, versus the radius, R, for H II regions on the envelope (black) and those regions below the envelope (grey).

Figure 8. Hα luminosity, $L_{H\alpha}$, versus H II size (radius, R) for isolated galaxies. The result of the double (or single) linear fit is drawn as a solid line. The n_e versus R of H II regions in isolated galaxies is plotted below each $L_{H\alpha}$–R plot.

Figure 8. – *continued*

Figure 8. – *continued*
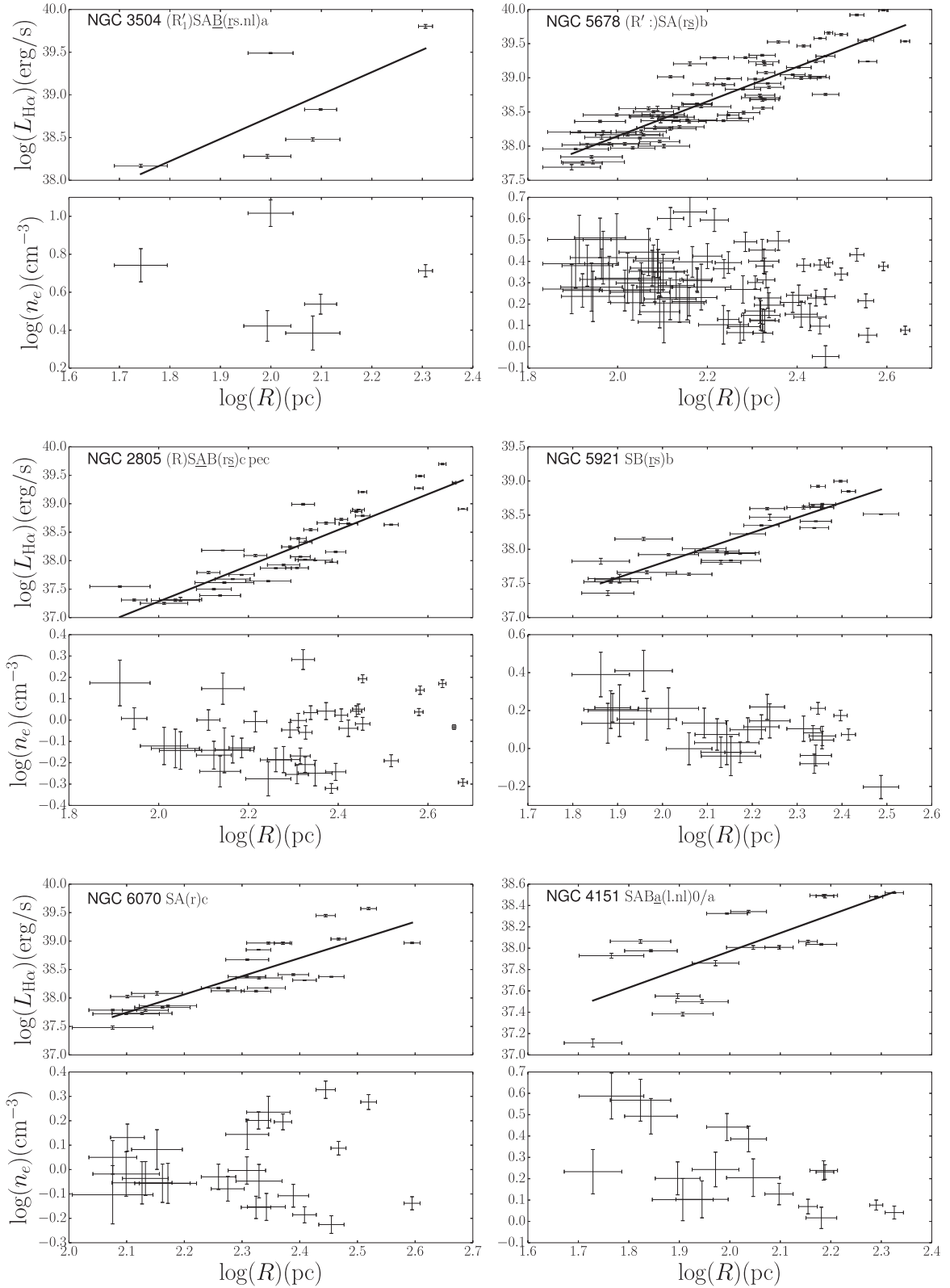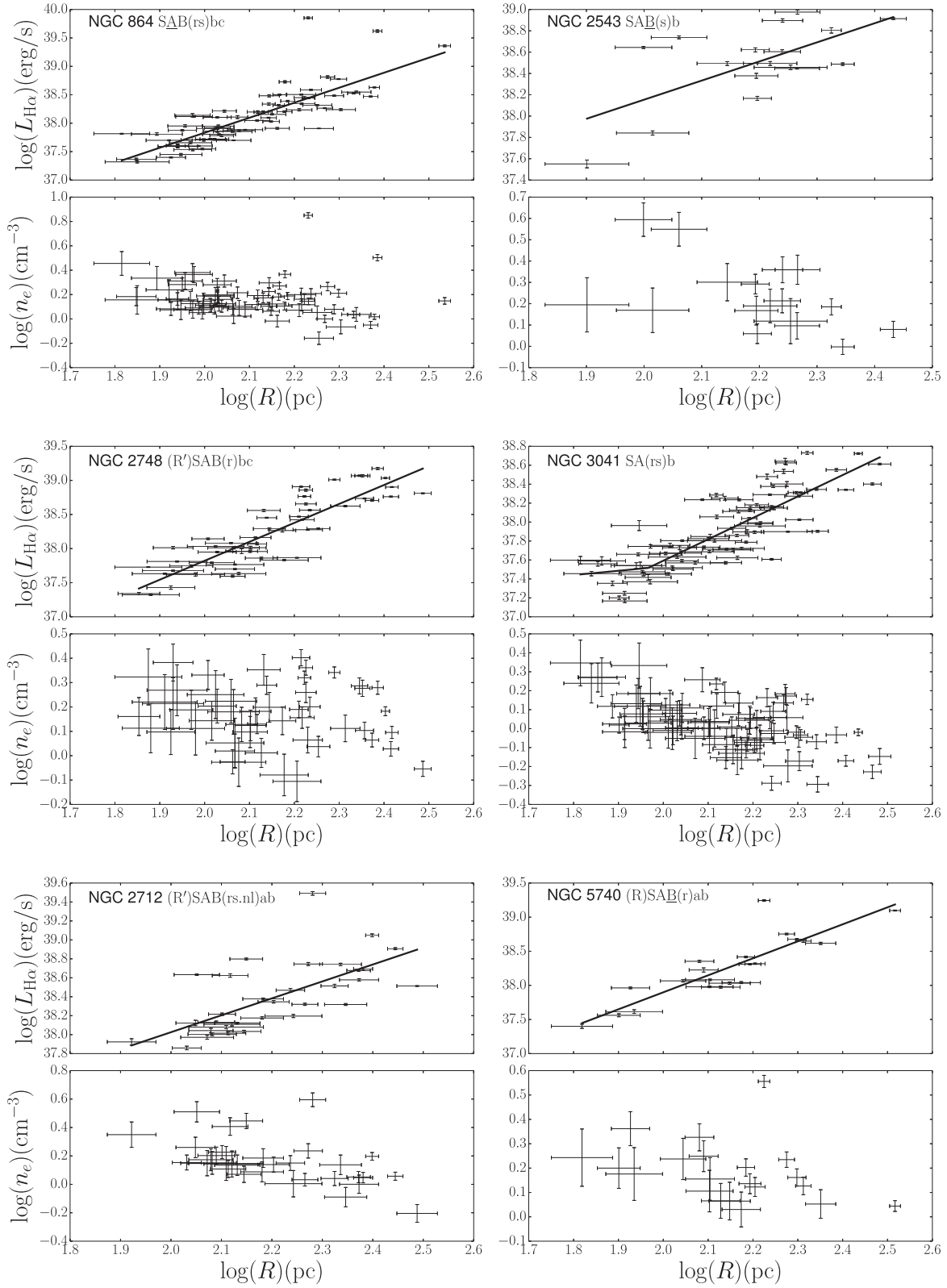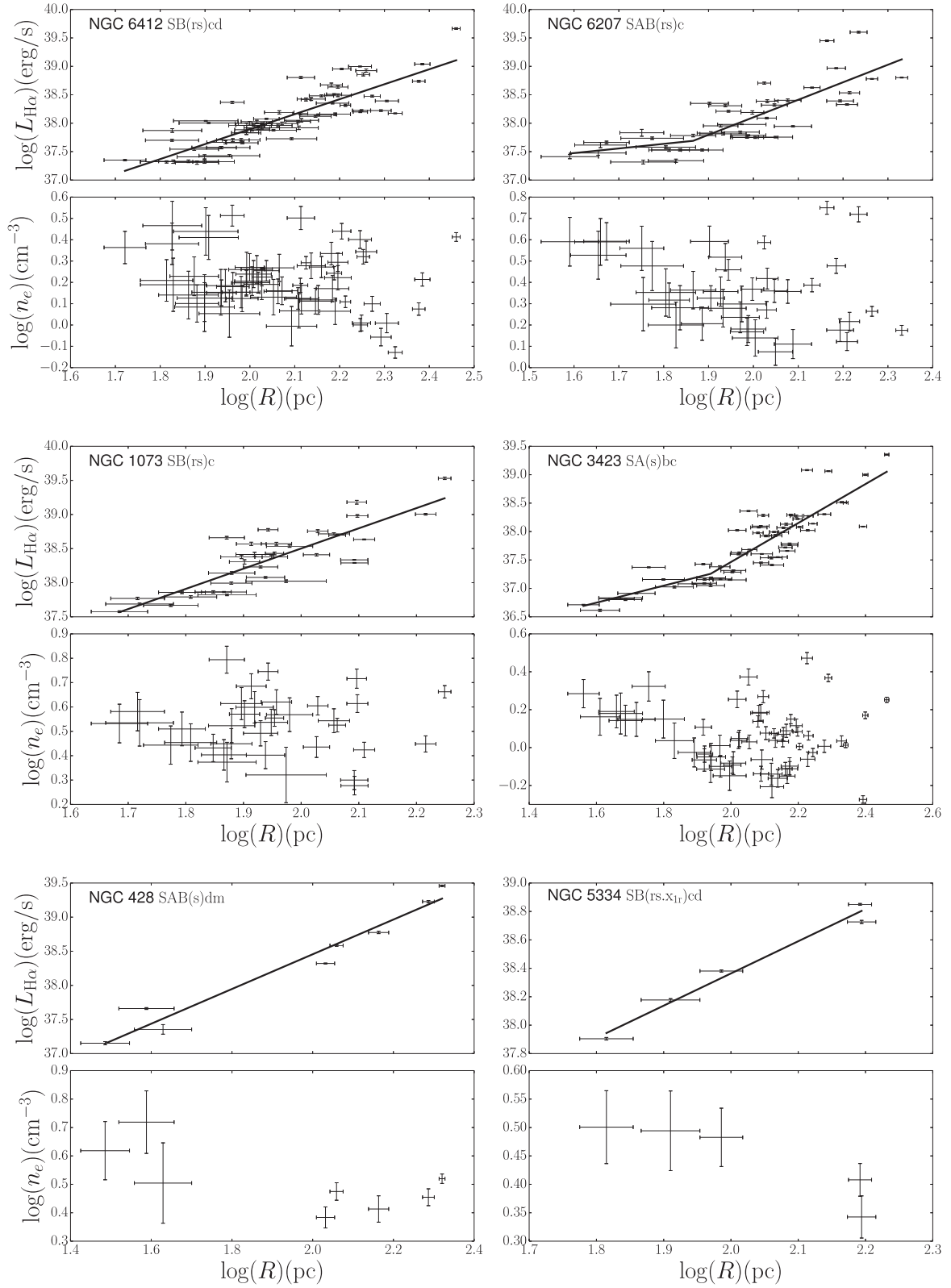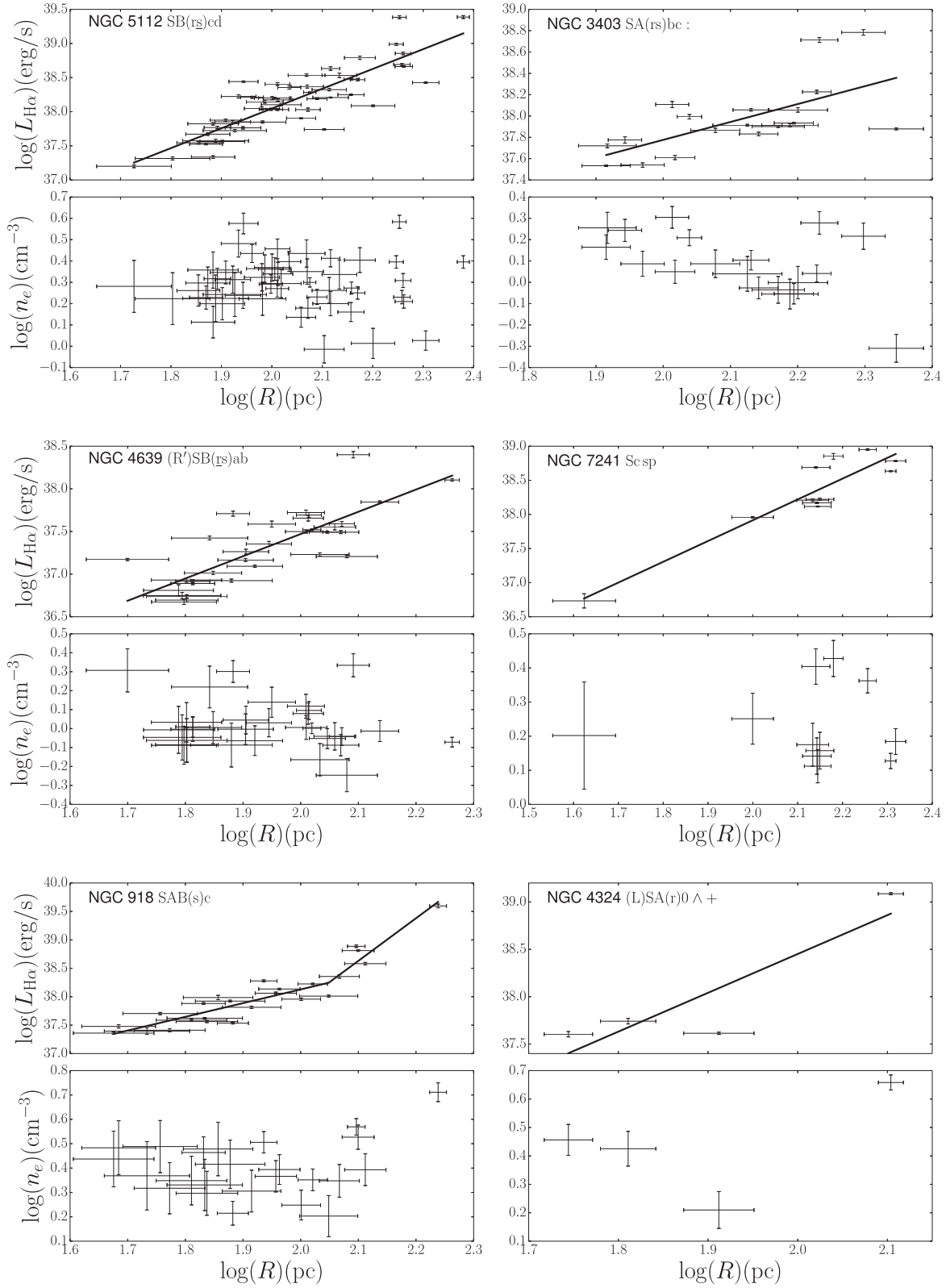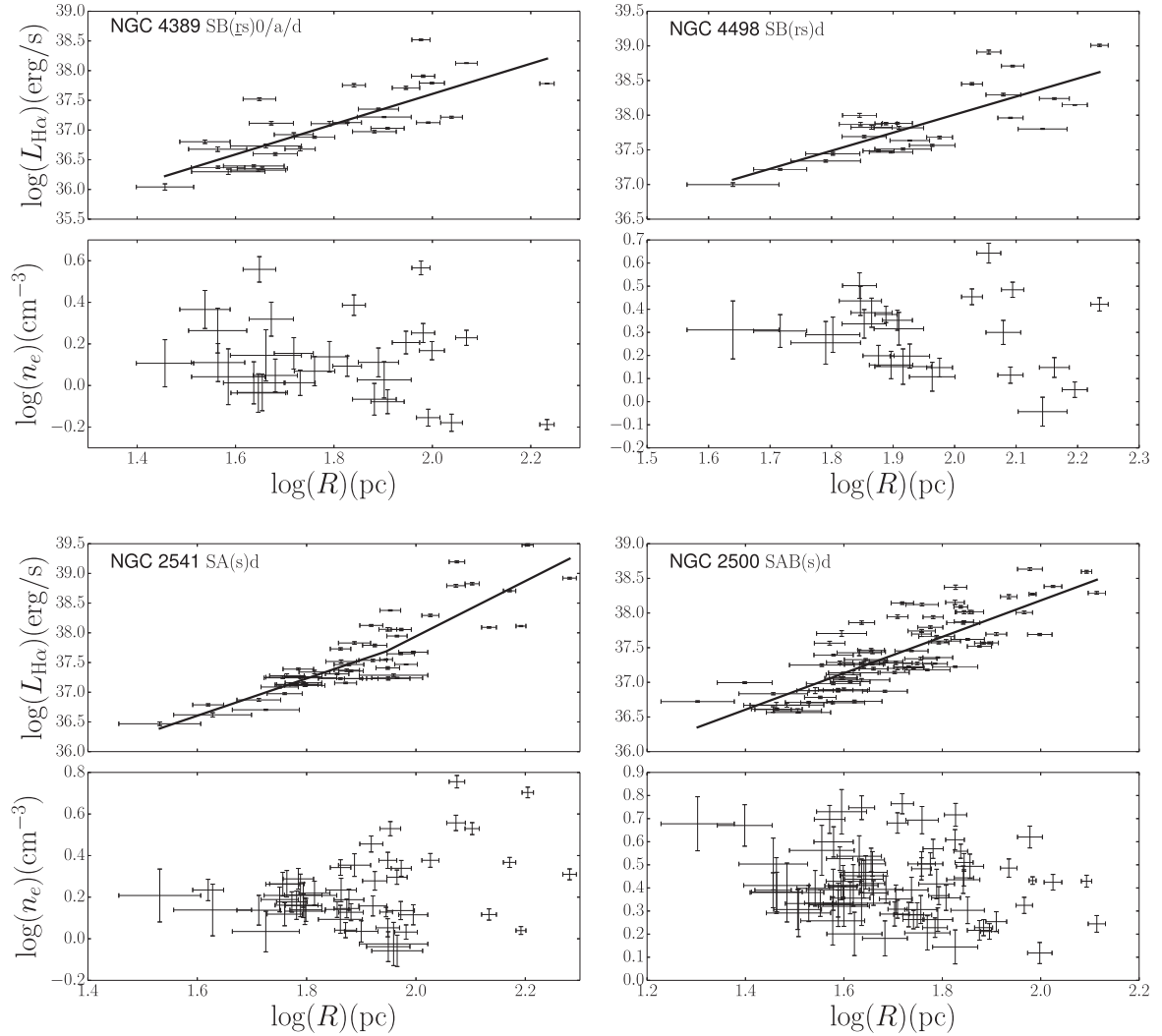
Figure 8. – *continued*

Figure 8. – *continued*

less frequent. Fig. 8 and Table 4 are sorted by absolute magnitude (see Erroz-Ferrer et al. 2015), from brighter to fainter. The regime where the exponent is larger than 3 is again independent on the absolute magnitude of the galaxy.

6.2 $L_{H\alpha}$–σ_v envelope

Following the same procedure as in the previous section in interacting galaxies, we plot the Hα luminosity versus velocity dispersion for H II regions in isolated galaxies in Fig. 9 (left). Again, we plot the envelope to the data

$$\log(L_{H\alpha\,\mathrm{env}}) = 2.0 \times \log(\sigma_v) + 37.6 \qquad (8)$$

implying that the SFR of the regions on the envelope depends superlinearly on the velocity dispersion.

We plot the electron density versus the radius of the regions, separating those regions on the envelope (black) from those regions below the envelope (grey) in Fig. 9 (right). For the set of isolated galaxies there is a deficiency of H II regions with a big enough velocity dispersion to be measured reliably by our observations, compared with H II regions in interacting galaxies. This is clear

when we compare Figs 6 (left) and 9 (left). We conclude that the velocity dispersions in the H II regions of interacting galaxies are larger presumably due to star formation feedback effects which enhance the dispersion.

For the isolated galaxies we cannot detect the two regimes in the electron density–radius relation when we separate the regions on and below the envelope because we do not have enough regions below the envelope (Fig. 9, right), implying that the effects of star formation feedback are significantly less than for the interacting galaxies, as we would expect.

6.3 Virial parameter

We plot the virial parameter versus Hα luminosity in Fig. 10. We see the same general behaviour as before, for the H II regions in isolated galaxies the virial parameter decreases with luminosity, implying that the brightest H II regions are dominated by self-gravity rather than being pressure confined. However, we can see that there is clearly a smaller proportion of H II regions in the brighter regime compared to the number of H II regions in the brighter regime in interacting galaxies.

Table 4. Results of the single and double (when applicable) linear fits for isolated galaxies. as defined in equation (6).

Name	N_1	L_1	N_2	L_2	$\log R_1$
NGC 3504	2.6	33.5			
NGC 5678	2.5	33.0			
NGC 2805	3.1	30.9			
NGC 5921	2.2	33.4			
NGC 6070	3.1	31.0			
NGC 4151	1.7	34.5			
NGC 864	2.6	32.5			
NGC 2543	1.7	34.5			
NGC 2748	2.7	32.2			
NGC 3041	0.4	36.6	2.2	33.0	1.9
NGC 2712	1.7	34.4			
NGC 5740	2.4	32.9			
NGC 6412	2.6	32.6			
NGC 6207	0.8	36.1	3.0	31.9	1.8
NGC 1073	2.9	32.5			
NGC 3423	1.4	34.3	3.4	30.6	1.9
NGC 428	2.5	33.3			
NGC 5334	2.2	33.8			
NGC 5112	2.9	32.2			
NGC 3403	1.6	34.4			
NGC 4639	2.6	32.2			
NGC 7241	3.0	31.8			
NGC 918	2.4	33.3	7.4	22.8	2.0
NGC 4324	4.0	30.2			
NGC 4389	2.5	32.5			
NGC 4498	2.6	32.8			
NGC 2541	3.1	31.5	4.6	28.6	1.9
NGC 2500	2.6	32.9			

7 COMPARISON

We have studied the differences in the populations of H II regions in the two samples of galaxies. We have plotted the H II region luminosity functions for interacting galaxies and isolated galaxies, which are well represented by a power law

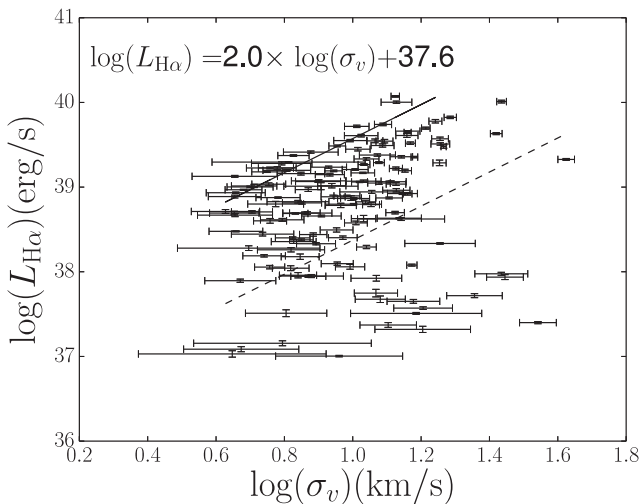$$N(L)\mathrm{d}L = AL^a\mathrm{d}L, \qquad (9)$$

Figure 9. Left: Hα luminosity, $L_{H\alpha}$, versus velocity dispersion, σ_v, for H II regions in isolated galaxies. We have plotted the fitted envelope as a solid line, and the displaced envelope condition explained in the text, as a dashed line. Right: n_e versus R for H II regions on the envelope (black) and those regions below the envelope (grey).
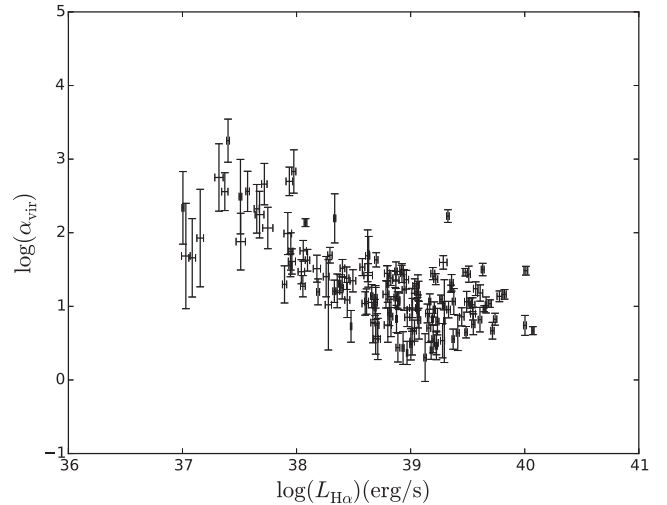
Figure 10. The virial parameter, $\alpha_{\mathrm{vir}} = 5\frac{\sigma_v^2 R_{H II}}{GM_{\mathrm{gas}}}$ versus Hα luminosity, $L_{H\alpha}$. We have used for the gas mass, the ionized gas, $M_{\mathrm{gas}} = M_{H II}$.

where $N(L)\mathrm{d}L$ is the number of H II regions with luminosity in the range $[L, L + \mathrm{d}L]$. Kennicutt et al. (1989), Beckman et al. (2000) and Bradley et al. (2006) showed that for a galaxy with a sufficiently large population of H II regions, the luminosity function is best fitted by a double power-law.

We plot the H II region luminosity functions in Fig. 11, showing in blue the H II regions of the interacting galaxies, and in red those of the isolated galaxies, as well as the double power-law fits.

We have estimated the completeness in both samples dividing each sample into two subsamples characterized by the distance to the galaxies. Thus, we have two subsamples for two ranges of smaller and larger distances, respectively, and we estimated the completeness limit where the slope of the luminosity function converge to the same value for both subsamples. The completeness limit for interacting galaxies is $L_{H\alpha} = 37.3$ dex while for isolated galaxies it is $L_{H\alpha} = 38$ dex.

For consistency with previous studies, we need to subtract 1 from the slopes of the fits in Fig. 11 to estimate the a value appearing
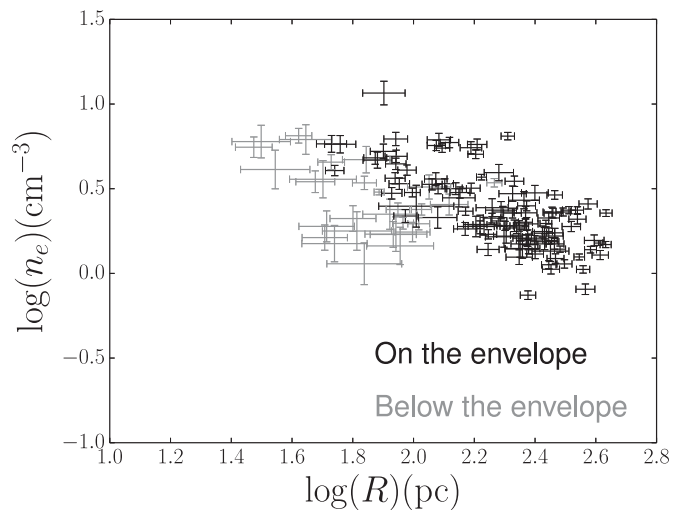
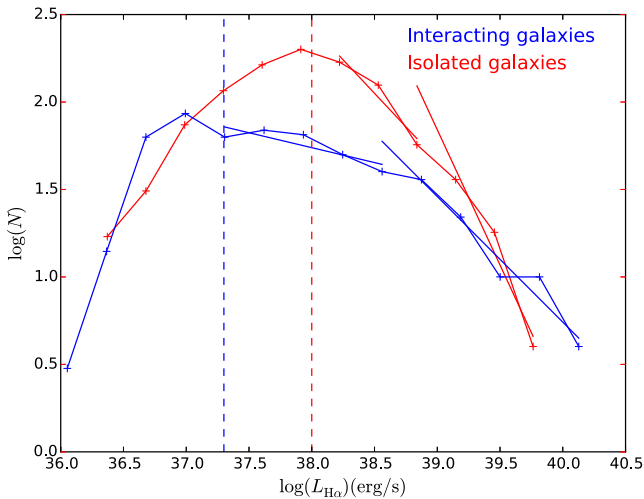**Figure 11.** H II region luminosity function for interacting galaxies (blue) and isolated galaxies (red). The completeness limit is drawn as a dashed vertical line in blue for interacting galaxies, and in red for isolated galaxies. The double fit is plotted as a solid line in blue for interacting galaxies, and in red for isolated galaxies.

in equation (9) since we have binned the data in logarithmic bins rather than linear bins. The results of the exponent in the luminosity function fit are

$$a = (-1.17 \pm 0.10)\,; \quad \text{for } \log(L_{H\alpha}) \leqslant 38.6\,\text{dex}$$
$$a = (-1.71 \pm 0.17)\,; \quad \text{for } \log(L_{H\alpha}) > 38.6\,\text{dex} \qquad (10)$$

for interacting galaxies, while for isolated galaxies the result is

$$a = (-1.8 \pm 0.2)\,; \quad \text{for } \log(L_{H\alpha}) < 38.8\,\text{dex}$$
$$a = (-2.5 \pm 0.3)\,; \quad \text{for } \log(L_{H\alpha}) > 38.8\,\text{dex.} \qquad (11)$$

We draw the conclusion that the H II region luminosity functions for the two samples are different within the uncertainties. The H II region population in the interacting galaxies is generally brighter in Hα (and therefore the SFR($L_{H\alpha}$) is higher) compared to isolated galaxies. The break in the luminosity function is compatible with those found in previous studies (Kennicutt et al. 1989; Bradley et al. 2006; Zaragoza-Cardiel et al. 2013, 2014). Zaragoza-Cardiel et al. (2013, 2014) claimed that this double population of H II regions

is due to different scaling relations in the $L_{H\alpha}$–R relation. In this study the break in the scaling relation for different galaxies is not constant due to the scatter in the data from which the change in scaling relations is derived.

We have applied the statistical Kolmogorov–Smirnov (K–S) test to derive the probability that the Hα luminosity distributions we have obtained for interacting and isolated galaxies are the same. The result is a probability of 10^{-4} per cent. We can therefore conclude that the Hα luminosity distribution in the sample of interacting galaxies is different from that of the isolated galaxies sample, and as Fig. 11 shows, that the H II regions interacting galaxies are brighter compared to those in isolated galaxies, because the luminosity function extends to higher values of the luminosity.

We plot the distribution of n_e in Fig. 12 (left). We can roughly compare the ionized gas density, n_e, with the molecular gas density (Zaragoza-Cardiel et al. 2014). The gas density in the H II regions from the interacting galaxies sample is clearly enhanced compared to those in the isolated galaxies. Since the SFR depends superlinearly on the gas density, the enhancement in the gas density in the interacting galaxies sample implies a strong enhancement in the SFR, and indeed of the star formation efficiency.

We commented in the previous section that there is a deficiency of H II regions with enough velocity dispersion to be measured by our observations. We also plot the distribution of σ_v in Fig. 12 (right) where we can see that the interaction of galaxies increases the turbulence in H II regions. The two main mechanisms which can contribute to produce this effect are, first the continued accretion of gas on to the H II regions even after the first massive stars have been formed, producing more massive regions, and therefore increasing the turbulence. The other mechanism is the star formation feedback by stellar winds and supernova explosions, implying that the feedback is stronger in galaxy interactions due to higher rates of star formation, and also the formation of more massive stars.

7.1 Age distribution of H II regions

Using the Hα narrow band and continuum observations made with ACAM, we estimate the Hα equivalent widths, EW, of the H II regions extracted in this study, in the same way as in Zaragoza-Cardiel et al. (2013, 2014). Assuming a direct relation between EW(Hα)
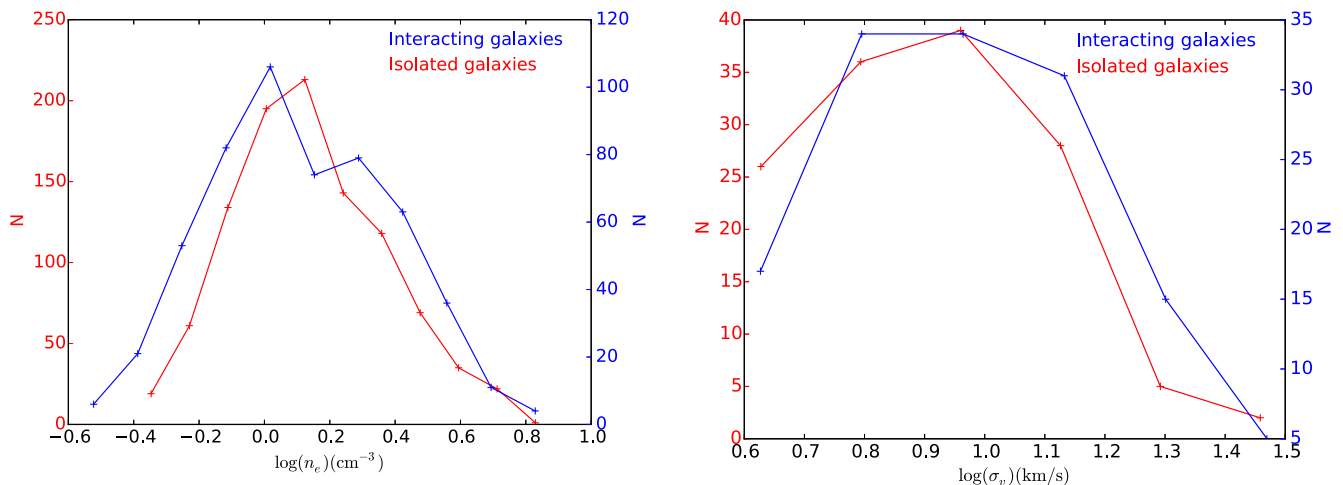
Figure 12. Left: distribution of electron densities n_e in H II regions of interacting galaxies (blue) and isolated galaxies (red). Right: distribution of velocity dispersion σ_v in H II regions of interacting galaxies (blue) and isolated galaxies (red). In both figures we plot two scales, one in blue at the right for interacting galaxies, and one at the left for isolated galaxies, in order to easily compare the different distributions.
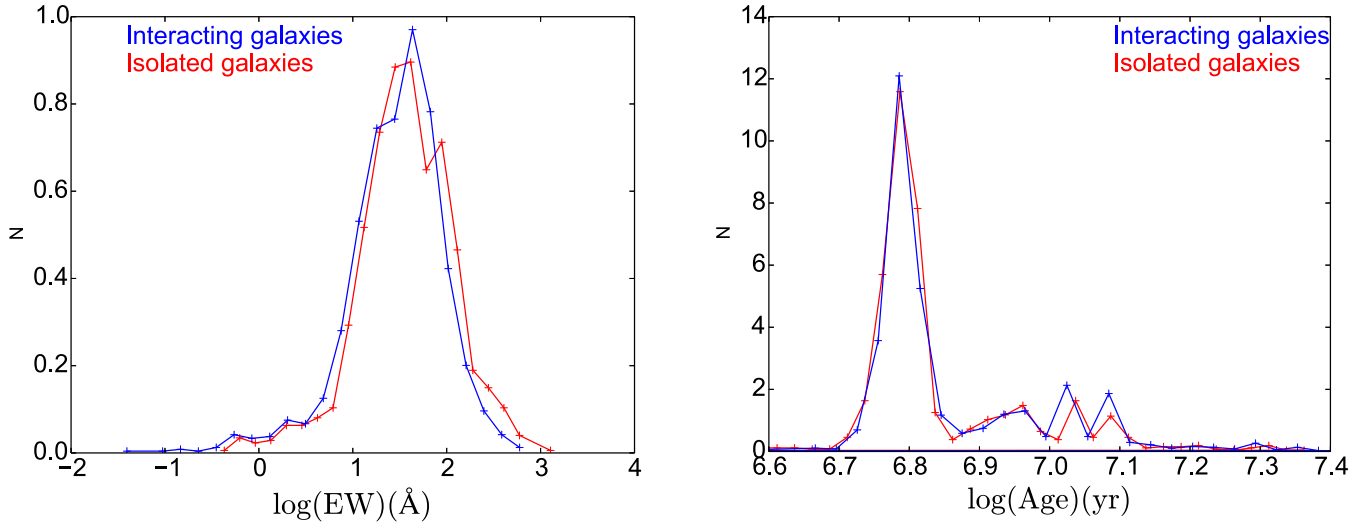
Figure 13. Left: normalized distribution of H II region equivalent widths, EW. Right: normalized distribution of ages (under the assumption of instantaneous star formation) derived using the equivalent width and STARBURST99 model (Leitherer et al. 1999).

and the age of the region (Leitherer et al. 1999), we derive also the age of the H II regions in this study, assuming solar metallicity and instantaneous star formation. The results are included in Tables A1 and A2. We plot the normalized distribution of EWs and ages in Fig. 13 (left and right, respectively). The histograms for the interacting and the isolated galaxies coincide, so there is no differentiation of the age distributions of H II regions in interacting and isolated galaxies. This could be taken as a point against our result of triggered star formation in interacting galaxies since the H II regions are forming on the same time-scales for both samples of galaxies. However, the age range in the distribution traced by Hα EW is much smaller than the typical merger time-scale, ∼ Gyr (Conselice 2009).

8 OFF-NUCLEAR PEAKS OF STAR FORMATION

Galaxy interactions produce a reduction in axisymmetry, causing gas flows towards the central parts of galaxies (Keel et al. 1985; Mihos & Hernquist 1996; Bournaud 2011), giving a well understood explanation of the nuclear starbursts observed in interacting galaxies. However, there are many examples of merging galaxies where there are intense star-forming regions at sites away from the nuclei of the two galaxies (Smith et al. 2007; Bournaud 2011), such as NGC 4038/9 (the Antennae galaxies), and NGC 4676 (the Mice).

The two populations of H II regions seem to be related to two underlying populations of Giant Molecular Clouds (GMCs) which are converted to ionized gas having similar mass distributions as the placental molecular gas (Zaragoza-Cardiel et al. 2014), at least in the more massive regions.

We can imagine an inflow in a galaxy induced by the interaction with a companion galaxy, with velocity, v_{in}, towards the central parts, since galaxy interactions can produce gas inflows. If a gas cloud is close to the inflow trajectory, the gas of the inflow will be accreted if the escape velocity, v_{esc}, from the gas cloud is larger than the velocity of the inflow, v_{in}.

In order to estimate the escape velocity of the gas inflow from the gas cloud, we use a very simplistic model where we neglect the influence of the galaxy which is producing the inflow towards the centre. A more realistic model in which the competing gravitational

pulls of the cloud towards its centre and of the galaxy towards its centre would give more accurate results, but is outside the scope of the this paper. However, it is easy to show that for a major fraction of the original galactic disc the galactocentric force is significantly less than the perturbing force of individual clouds with radii greater than, say, 50 pc so the results presented here can be taken as qualitatively valid. The escape velocity from the surface of a gas cloud is

$$v_{esc} = \sqrt{\frac{2\,G\,M}{b}}, \qquad (12)$$

where b is the impact parameter of the inflow with respect to the centre of the cloud. Let us assume that the mass of a region is related to the radius by $M(R) = M_0\,R^N$, then

$$v_{esc} = \sqrt{\frac{2\,G\,M_0\,R^N}{b}} = v_0\,R^{\frac{N}{2}}. \qquad (13)$$

We have seen that for the H II regions we can divide the scaling relations between luminosity and radius into two. The regions with high luminosity, significantly more abundant in the interacting galaxies, show exponents of 3 or greater, while the regions with lower luminosity show exponents closer to 2. Previous work on molecular clouds has shown (Kauffmann et al. 2010; Lombardi, Alves & Lada 2010; Roman-Duval et al. 2010; Colombo et al. 2014) that molecular clouds in general have a relation between gas mass and cloud radius with an exponent close to 2, which is consistent with the value found by Larson (1981), frequently quoted as one of the Larson laws. For the interacting galaxy pair the Antennae, Zaragoza-Cardiel et al. (2014) found an exponent of 2.6 for the mass–radius relation of its most massive molecular clouds. It is straightforward to show that if the Larson law relating the velocity dispersion σ_v to the cloud mass $M_\odot$, ($\sigma_v \propto M^{0.2}$), holds good, for a sequence of molecular clouds of increasing mass where the exponent in the mass–radius relation is 2 or greater, there will be a mass above which the clouds become gravitationally bound. In Zaragoza-Cardiel et al. (2014) we showed that this would account for the tendency of the virial parameter to approach unity for molecular clouds of high enough mass (for the Antennae this implies cloud masses greater than some $10^{6.5}$ $M_\odot$). We also argued that any clouds with masses of this order in the galaxies prior to interaction would tend to accrete mass from the gas flows induced
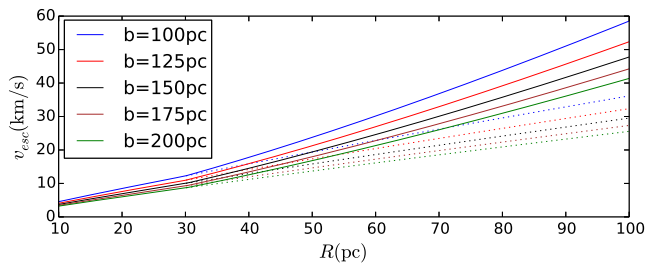
Figure 14. Escape velocity, $v_{\rm esc}$, of the clouds as a function of their radius, R, for different values of the impact parameter, b. The solid lines represent the case of a double regime in the mass–radius relation (equation 14) while the dotted lines represent the case of the single mass–radius relation with a canonical exponent of $N = 2$.

by the interaction. To pursue this argument further we can estimate, using somewhat simplified assumptions, the escape velocity as a function of cloud size, taking two different scaling relations, one for the lower mass clouds, and the other for the high-mass clouds. The corresponding relations can be expressed as

$$M = 3817R^2; \text{ for } R < 30\,{\rm pc}$$
$$M = 251R^{2.61}; \text{ for } R > 30\,{\rm pc}. \tag{14}$$

We introduce equation (14) into equation (13) for different impact parameters obtaining the plots shown in Fig. 14, where we can clearly see the escape velocity enhancement in the case of the double mass–radius regime (solid lines) compared to the case of single mass–radius regime (dotted lines).

An inflow of gas of $v_{\rm in} = 27\ {\rm km\,s^{-1}}$ was observed for the interacting galaxy NGC 3396 (Zaragoza-Cardiel et al. 2013). As an example, with this gas inflow velocity value we can conclude from Fig. 14 that regions with radius larger than $\sim$60 pc would accrete gas from the inflow in the double mass–radius regime, while only regions with radius larger than $\sim$80 pc would accrete gas in the single mass–radius regime. The latter may not be gravitationally bound prior to the merging process, but as they acquire more gas they become so.

We suggest that our study, showing that the largest clouds are bound by their own gravitation, strongly supports the scenario where the gas accreted from the flowing gas passing near these clouds (which are already present in the isolated galaxies prior to interaction) is the cause of the star formation enhancement in interacting galaxies and can give rise to the off-nuclear peaks of star formation. Thus, although we still do not, at this stage, have a model for how the gravitationally dominated gas clouds form initially within the pre-merging galaxies, the inflow of gas in the interacting galaxies from the outer parts should increment the number of gravitationally dominated clouds.

9 CONCLUSIONS

We have presented new Fabry–Perot observations for 10 interacting galaxies: the Hα surface brightness, velocity dispersion and velocity dispersion maps. All of these values are available through CDS. We have amalgamated our tables of the properties of H II regions for the sample of interacting galaxies presented here together with two interacting systems, Arp 270, and the Antennae galaxies from our previous publications (Zaragoza-Cardiel et al. 2013, 2014). We give here the catalogue of 1259 H II regions, including the radius, Hα luminosity, velocity dispersion, electron density, ionized gas mass, the virial parameter and the corresponding errors for each parameter.

In order to compare the properties of H II regions in interacting galaxies with those in isolated galaxies, we have included the parameters of H II regions in a sample of 28 isolated galaxies observed with the same instrument (Erroz-Ferrer et al. 2015), obtaining these parameters (the same as those for the interacting galaxies) for 1054 H II regions. We present a subsample of the brightest H II regions of the catalogue in Table A1 in for the interacting galaxies, and in Table A2 for the isolated galaxies. The full catalogues of the H II region samples are available as a machine readable table in the electronic version of the article, as well as through CDS.

The scaling relations, $L_{\rm H\alpha}$–R, obtained here for interacting galaxies are different from previous studies for isolated galaxies (Terlevich & Melnick 1981; Gutiérrez & Beckman 2010b) in most of the cases, and in agreement with recent results for the two interacting systems whose H II regions we have included here (Zaragoza-Cardiel et al. 2013, 2014). They differ in the exponent of the relation $L_{\rm H\alpha} \propto R^N$. We have found that for almost all the interacting galaxies, the $L_{\rm H\alpha}$–R is best represented by a double line, one for the smallest H II regions ($\lesssim$ 100pc) similar to previous studies where the exponent N is smaller than 3, and other for the largest H II regions ($\gtrsim$ 100pc) where the exponent N is larger than 3, except for two galaxies where we do not have enough fainter H II regions to fit a double linear fit and we find that the exponent N is larger than 3, independently of the radius. If $N > 3$, then the electron (or the ionized gas mass) density derived from equations (4) and (5) increases with size, in contrast with previous results in isolated galaxies where the electron density in H II regions decreases with size (Terlevich & Melnick 1981; Gutiérrez & Beckman 2010b).

In the sample of isolated galaxies, we have found that the scaling relation $L_{\rm H\alpha}$–R is similar to that found in previous studies in 22 of our 28 isolated galaxy sample, with slopes smaller than 3.

The differences in the exponents of the $L_{\rm H\alpha}$–R relation are independent of the absolute magnitude of the galaxies.

The $L_{\rm H\alpha}$–σ_v plot shows an envelope which has been detected in a previous published work, whose authors suggested that the regions on this envelope are virialized (Relaño et al. 2005). In the case of interacting galaxies, the regions on the envelope are the ones where the gas density increases with size. In the case of isolated galaxies we do not have sufficient regions with large enough velocity dispersion to reach a clear conclusion. The Hα luminosity, and the derived SFR of the H II regions on the envelope depend superlinearly on the velocity dispersion. We have obtained the virial parameter $\alpha_{\rm vir}$ which is an estimate of the ratio between the kinetic and the gravitational energy (Bertoldi & McKee 1992), and have used this to show that the brighter the region, the more clearly it is held together by self gravity rather than external pressure.

We have quantified the differences between the two populations of H II regions, those from interacting galaxies, and those from the isolated galaxies. Comparing the luminosity functions we find that the H II regions in the interacting galaxies are on average brighter than the H II regions from the isolated galaxies. The K–S test performed on the two distributions of Hα luminosities gives a probability of 10^{-4} per cent for the hypothesis that the two populations of H II regions are really the same.

The histograms of electron density and velocity dispersion show that on average the H II regions from interacting galaxies are denser and more turbulent than those from isolated galaxies. Since the SFR depends superlinearly on gas density, the enhancement in the gas density in interacting galaxies implies a significant enhancement in the star formation efficiency.

However, the distributions of equivalent widths and ages of H II region coincide for the two samples of galaxies, showing that the

formation of the young massive stellar component traced by Hα extends over a similar range in time for interacting and isolated galaxies.

However, the sample of interacting galaxies is, on average, brighter than that of the isolated galaxies. We could conclude that the presence of the population of brighter H II regions in the interacting galaxies might be simply due to their greater masses. Nevertheless, the number of H II regions in an interacting galaxy is bigger than the number in an isolated galaxy with the same absolute magnitude, suggesting that interactions do in fact increase the SFR.

Based on the results from Wei, Keto & Ho (2012) and Zaragoza-Cardiel et al. (2014), we claim that the two populations of H II regions are related to two populations of GMCs. Romeo & Agertz (2014) claim that Toomre stability criteria depends on the values of exponents in the Larson laws. In the case of the exponent in the mass–size relation, largest values of this exponent imply that larger scales are unstable, in agreement with the presence of larger star-forming regions in the high-mass regime. The presence of massive clumps of star formation in nearby galaxies as those studied here can improve our understanding about the clumpy star-forming discs observed at higher redshifts (Elmegreen et al. 2007).

We claim that the brightest and most massive star-forming regions can accrete gas that is inflowing towards the central parts of the galaxies, or has suffered a perturbation in its original orbit, induced by interactions. Blasco-Herrera et al. (2013) found in their sample of 11 starburst galaxies that 8 of them show evidence of a recent merger while they are still dominated by rotation, in agreement with a picture where the interactions trigger flows and star formation without messing up the host galaxy's kinematics. This could be a plausible scenario for the off-nuclear peaks of star formation produced in galaxy collisions, a scenario which requires further observational and theoretical exploration.

REFERENCES

Arp H., 1966, ApJS, 14, 1
Astropy Collaboration et al., 2013, A&A, 558, A33
Beckman J. E., Rozas M., Zurita A., Watson R. A., Knapen J. H., 2000, AJ, 119, 2728
Benn C., Dee K., Agócs T., 2008, in McLean I. S., Casali M. M., eds, Proc. SPIEConf. Ser. Vol. 7014, Ground-based and Airborne Instrumentation for Astronomy II. SPIE, Bellingham, p. 70146X
Bennert N., Canalizo G., Jungwiert B., Stockton A., Schweizer F., Peng C. Y., Lacy M., 2008, ApJ, 677, 846
Bertoldi F., McKee C. F., 1992, ApJ, 395, 140
Bessiere P. S., Tadhunter C. N., Ramos Almeida C., Villar-Martín M., 2012, MNRAS, 426, 276
Blasco-Herrera J. et al., 2010, MNRAS, 407, 2519
Blasco-Herrera J., Fathi K., Östlin G., Font J., Beckman J. E., 2013, MNRAS, 435, 1958
Bournaud F., 2011, Eur. Astron. Soc. Publ. Ser., 51, 107
Bournaud F., Elmegreen B. G., Teyssier R., Block D. L., Puerari I., 2010, MNRAS, 409, 1088
Bradley T. R., Knapen J. H., Beckman J. E., Folkes S. L., 2006, A&A, 459, L13
Brandl B. R. et al., 2005, ApJ, 635, 280
Calzetti D., Harris J., Gallagher J. S., III, Smith D. A., Conselice C. J., Homeier N., Kewley L., 2004, AJ, 127, 1405
Camps-Fariña A., Zaragoza-Cardiel J., Beckman J. E., Font J., García-Lorenzo B., Erroz-Ferrer S., Amram P., 2015, MNRAS, 447, 3840
Canalizo G., Bennert N., Jungwiert B., Stockton A., Schweizer F., Lacy M., Peng C., 2007, ApJ, 669, 801
Cedrés B., Beckman J. E., Bongiovanni Á., Cepa J., Asensio Ramos A., Giammanco C., Cabrera-Lavers A., Alfaro E. J., 2013, ApJ, 765, LL24
Chávez R., Terlevich R., Terlevich E., Bresolin F., Melnick J., Plionis M., Basilakos S., 2014, MNRAS, 442, 3565
Chu Y.-H., Kennicutt R. C., Jr, 1994, ApJ, 425, 720
Cisternas M. et al., 2011, ApJ, 726, 57
Colombo D. et al., 2014, ApJ, 784, 3
Conselice C. J., 2009, MNRAS, 399, L16
Daigle O., Carignan C., Hernandez O., Chemin L., Amram P., 2006, MNRAS, 368, 1016
de Vaucouleurs G., de Vaucouleurs A., Corwin H. G., Jr 1976, Second Reference Catalogue of Bright Galaxies., Univ. Texas Press, Austin, TX
Dyson J. E., 1979, A&A, 73, 132
Elmegreen D. M., Elmegreen B. G., Ravindranath S., Coe D. A., 2007, ApJ, 658, 763
Erroz-Ferrer S. et al., 2012, MNRAS, 427, 2938
Erroz-Ferrer S. et al., 2015, preprint (arXiv:1504.06282)
Georgakakis A. et al., 2009, MNRAS, 397, 623
Giammanco C., Beckman J. E., Zurita A., Relaño M., 2004, A&A, 424, 877
Gutiérrez L., Beckman J., 2010a, The Impact of HST on European Astronomy. Springer-Verlag, Berlin, p. 77
Gutiérrez L., Beckman J. E., 2010b, ApJ, 710, L44
Gutiérrez L., Beckman J. E., Buenrostro V., 2011, AJ, 141, 113
Hernandez O. et al., 2008, PASP, 120, 665
Hippelein H., Fried J. W., 1984, A&A, 141, 49
Hong S. et al., 2011, ApJ, 731, 45
Hopkins P. F., Keres D., Onorbe J., Faucher-Giguère C.-A., Quataert E., Murray N., Bullock J. S.20142014, MNRAS, 445, 581
Karachentsev I., Lebedev V., Shcherbanovski A., 1985, Bull. Inf. Cent. Donnees Stellaires, 29, 87
Kauffmann J., Pillai T., Shetty R., Myers P. C., Goodman A. A., 2010, ApJ, 716, 433
Keel W. C., Kennicutt R. C., Jr, Hummel E., van der Hulst J. M., 1985, AJ, 90, 708
Kennicutt R. C., Jr, Edgar B. K., Hodge P. W., 1989, ApJ, 337, 761
Larson R. B., 1981, MNRAS, 194, 809
Leitherer C. et al., 1999, ApJS, 123, 3
Lombardi M., Alves J., Lada C. J., 2010, A&A, 519, L7
Mihos J. C., Hernquist L., 1996, ApJ, 464, 641
Paturel G., Petit C., Prugniel P., Theureau G., Rousseau J., Brouty M., Dubois P., Cambrésy L., 2003, A&A, 412, 45

Ramos Almeida C., Tadhunter C. N., Inskip K. J., Morganti R., Holt J., Dicken D., 2011, MNRAS, 410, 1550

Ramos Almeida C. et al., 2012, MNRAS, 419, 687

Relaño M., Beckman J. E., Zurita A., Rozas M., Giammanco C., 2005, A&A, 431, 235

Roman-Duval J., Jackson J. M., Heyer M., Rathborne J., Simon R., 2010, ApJ, 723, 492

Romeo A. B., Agertz O., 2014, MNRAS, 442, 1230

Rosa M., Solf J., 1984, A&A, 130, 29

Rosolowsky E., Leroy A., 2006, PASP, 118, 590

Rosolowsky E. W., Pineda J. E., Kauffmann J., Goodman A. A., 2008, ApJ, 679, 1338

Smith B. J., Struck C., Hancock M., Appleton P. N., Charmandaris V., Reach W. T., 2007, AJ, 133, 791

Smith B. J., Soria R., Struck C., Giroux M. L., Swartz D. A., Yukita M., 2014, AJ, 147, 60

Somerville R. S., Hopkins P. F., Cox T. J., Robertson B. E., Hernquist L., 2008, MNRAS, 391, 481

Spitzer L., 1978, Physical Processes in the Interstellar Medium. Wiley-Interscience Publ., New York, p. 333

Tadhunter C. et al., 2011, MNRAS, 412, 960

Terlevich R., Melnick J., 1981, MNRAS, 195, 839

Vorontsov-Velyaminov B. A., Noskova R. I., Arkhipova V. P., 2001, Astronomical and Astrophysical Transactions, 20, 717

Wei L. H., Keto E., Ho L. C., 2012, ApJ, 750, 136

White S. D. M., Rees M. J., 1978, MNRAS, 183, 341

Wisnioski E. et al., 2015, ApJ, 799, 209

Yang H., Chu Y.-H., Skillman E. D., Terlevich R., 1996, AJ, 112, 146

Zaragoza-Cardiel J. et al., 2013, MNRAS, 432, 998

Zaragoza-Cardiel J., Font J., Beckman J. E., García-Lorenzo B., Erroz-Ferrer S., Gutiérrez L., 2014, MNRAS, 445, 1412

Zurita A., Beckman J. E., Rozas M., Ryder S., 2002, A&A, 386, 801

SUPPORTING INFORMATION

Additional Supporting Information may be found in the online version of this article:

Table A1. Physical properties of the brightest H II regions in interacting galaxies derived as described in Section 4.
Table A2. Physical properties of the brightest H II regions in isolated galaxies derived as described in Section 4 (http://mnras.oxfordjournals.org/lookup/suppl/doi:10.1093/mnras/stv1024/-/DC1).

Please note: Oxford University Press is not responsible for the content or functionality of any supporting materials supplied by the authors. Any queries (other than missing material) should be directed to the corresponding author for the paper.

APPENDIX A: PROPERTIES OF THE H II REGIONS

Table A1. Physical properties of the brightest H II regions in interacting galaxies derived as described in Section 4. The whole table is available as a machine readable table in the electronic version of the paper and through CDS.

N	Galaxy	RA (hh:mm:ss)	Dec. (° ′ ″)	$\log(L_{H\alpha})$ (erg s^{-1})	$R_{H II}$ (pc)	$\log(M_{H II})$ (M$_\odot$)	$\rho_{H II}$ (M$_\odot$ pc^{-3})	σ_v (km s^{-1})	α_{vir}	EW$_{H\alpha}$ (Å)	log(Age) (yr)
1	NGC 2146	6:18:22.7	78:22:25.6	39.04 ± 0.04	114 ± 4	5.9 ± 0.06	0.127 ± 0.008	15.0 ± 1.0	40.0 ± 9.0	39.9	6.82
2	NGC 2146	6:18:31.1	78:21:39.6	38.83 ± 0.04	116 ± 4	5.8 ± 0.07	0.097 ± 0.007	17.0 ± 1.0	60.0 ± 10.0	117.71	6.78
1	Arp244	12:1:55.6	−18:52:52.0	40.2 ± 0.03	280 ± 5	7.06 ± 0.05	0.126 ± 0.006	32.8 ± 0.7	30.0 ± 3.0	202.62	6.76
2	Arp244	12:1:53.9	−18:52:42.7	39.97 ± 0.03	253 ± 6	6.88 ± 0.05	0.111 ± 0.006	19.1 ± 0.7	14.0 ± 2.0	63.77	6.8
1	NGC 520	1:24:35.6	3:47:19.0	39.12 ± 0.04	255 ± 9	6.46 ± 0.07	0.042 ± 0.003	14.1 ± 0.8	20.0 ± 4.0	2.1	7.19
2	NGC 520	1:24:35.5	3:47:30.2	38.57 ± 0.03	187 ± 8	5.99 ± 0.08	0.035 ± 0.003	<4.0		10.93	7.05
1	UGC3995	7:44:11.3	29:15:13.1	40.29 ± 0.04	270 ± 10	7.09 ± 0.08	0.14 ± 0.01	43.0 ± 3.0	50.0 ± 10.0	17.66	6.95
2	UGC3995	7:44:11.1	29:14:34.6	40.06 ± 0.06	390 ± 30	7.2 ± 0.1	0.064 ± 0.009	8.0 ± 1.0	1.7 ± 0.9	11.48	7.05
1	NGC 3788	11:39:42.5	31:54:34.0	39.7 ± 0.02	280 ± 10	6.81 ± 0.07	0.072 ± 0.005	11.9 ± 0.9	7.0 ± 2.0	23.29	6.88
2	NGC 3788	11:39:42.3	31:54:32.6	39.58 ± 0.04	200 ± 20	6.5 ± 0.1	0.1 ± 0.01	<4.0		14.92	7.02
1	NGC 3786	11:39:45.0	31:55:30.7	39.86 ± 0.02	300 ± 10	6.93 ± 0.08	0.078 ± 0.006	16.5 ± 0.7	11.0 ± 2.0	18.88	6.88
2	NGC 3786	11:39:45.3	31:55:24.0	39.69 ± 0.02	240 ± 10	6.71 ± 0.09	0.088 ± 0.008	7.0 ± 1.0	3.0 ± 1.0	8.79	7.09
1	NGC 2782	9:14:5.1	40:6:43.8	39.8 ± 0.02	166 ± 6	6.52 ± 0.07	0.17 ± 0.01	28.0 ± 3.0	40.0 ± 10.0	63.41	6.8
2	NGC 2782	9:14:4.1	40:6:47.2	39.34 ± 0.01	128 ± 5	6.12 ± 0.06	0.15 ± 0.01	21.0 ± 2.0	50.0 ± 10.0	21.63	6.96
1	NGC 2993	9:45:48.2	−14:22:7.8	40.07 ± 0.01	258 ± 7	6.94 ± 0.04	0.121 ± 0.005	12.0 ± 1.0	5.0 ± 1.0	135.88	6.78
2	NGC 2993	9:45:50.8	−14:23:48.2	39.21 ± 0.02	175 ± 9	6.26 ± 0.09	0.081 ± 0.007	<4.0		0.92	7.31
1	NGC 2992	9:45:42.5	−14:19:30.5	39.18 ± 0.05	100 ± 8	5.9 ± 0.1	0.18 ± 0.03	16.0 ± 3.0	40.0 ± 20.0	10.78	7.05
2	NGC 2992	9:45:42.2	−14:19:22.6	39.16 ± 0.04	127 ± 9	6.0 ± 0.1	0.12 ± 0.02	6.0 ± 2.0	5.0 ± 4.0	18.63	6.96
1	NGC 3991	11:57:29.6	32:19:49.4	40.44 ± 0.02	470 ± 8	7.52 ± 0.03	0.076 ± 0.003	20.9 ± 0.8	7.2 ± 0.9	47.72	6.81
2	NGC 3991	11:57:29.6	32:19:51.7	39.47 ± 0.02	350 ± 10	6.84 ± 0.06	0.039 ± 0.002	8.0 ± 0.7	<4.0 ± 1.0	68.51	6.8
1	Arp270	10:49:54.1	32:59:44.4	40.22 ± 0.04	229 ± 4	6.94 ± 0.05	0.175 ± 0.009	20.4 ± 0.9	13.0 ± 2.0	2.43	7.17
2	Arp270	10:49:50.4	32:59:2.4	40.15 ± 0.04	146 ± 2	6.62 ± 0.05	0.31 ± 0.01	35.0 ± 1.0	49.0 ± 7.0	96.73	6.79
1	NGC 3769	11:37:51.8	47:52:46.4	38.31 ± 0.05	66 ± 3	5.17 ± 0.09	0.12 ± 0.01	<4.0		227.02	6.76
2	NGC 3769	11:37:51.0	47:52:51.5	38.14 ± 0.05	70 ± 4	5.1 ± 0.1	0.09 ± 0.01	<4.0		148.42	6.77

Table A2. Physical properties of the brightest H II regions in isolated galaxies derived as described in Section 4. The whole table is available as a machine readable table in the electronic version of the paper and through CDS.

N	Galaxy	RA (hh:mm:ss)	Dec. (° ′ ″)	$\log(L_{H\alpha})$ (erg s^{-1})	R_{HII} (pc)	$\log(M_{HII})$ (M$_\odot$)	ρ_{HII} (M$_\odot$ pc^{-3})	σ_v (km s^{-1})	α_{vir}	EW$_{H\alpha}$ (Å)	log(Age) (yr)
1	NGC 3504	11:3:10.4	27:58:59.4	39.61 ± 0.04	162 ± 5	6.41 ± 0.06	0.145 ± 0.009	14.4 ± 0.9	15.0 ± 3.0	17.03	6.98
2	NGC 3504	11:3:10.0	27:58:47.2	39.3 ± 0.01	80 ± 7	5.8 ± 0.1	0.29 ± 0.04	6.0 ± 3.0	6.0 ± 7.0	17.89	6.96
1	NGC 5678	14:32:12.6	57:53:49.0	40.07 ± 0.02	430 ± 9	7.28 ± 0.04	0.057 ± 0.002	13.3 ± 0.3	4.7 ± 0.5	29.49	6.83
2	NGC 5678	14:32:5.8	57:55:6.5	40.0 ± 0.03	380 ± 10	7.15 ± 0.08	0.064 ± 0.004	13.0 ± 1.0	6.0 ± 1.0	5.58	7.1
1	NGC 5921	15:21:56.6	5:4:12.4	39.22 ± 0.02	320 ± 10	6.67 ± 0.06	0.033 ± 0.002	<4.0		1.99	7.2
2	NGC 5921	15:21:53.6	5:3:22.3	39.15 ± 0.03	289 ± 9	6.56 ± 0.06	0.036 ± 0.002	<4.0		16.31	7.0
1	NGC 6070	16:9:55.2	0:42:3.3	39.57 ± 0.04	331 ± 9	6.86 ± 0.06	0.047 ± 0.003	18.0 ± 0.9	17.0 ± 3.0	79.3	6.8
2	NGC 6070	16:9:56.4	0:42:27.8	39.45 ± 0.04	279 ± 9	6.68 ± 0.07	0.053 ± 0.004	10.4 ± 0.7	7.0 ± 2.0	120.82	6.78
1	NGC 4151	12:10:32.6	39:24:21.1	38.21 ± 0.01	148 ± 5	5.65 ± 0.06	0.033 ± 0.002	<4.0		126.03	6.78
2	NGC 4151	12:10:32.6	39:24:20.8	38.18 ± 0.02	107 ± 6	5.43 ± 0.09	0.052 ± 0.005	<4.0		138.64	6.78
1	NGC 864	2:15:27.6	6:0:8.8	40.01 ± 0.03	204 ± 4	6.76 ± 0.04	0.162 ± 0.007	27.2 ± 0.8	30.0 ± 4.0	54.09	6.81
2	NGC 864	2:15:28.7	6:0:43.3	39.78 ± 0.04	291 ± 6	6.88 ± 0.05	0.073 ± 0.004	17.5 ± 0.7	14.0 ± 2.0	27.61	6.83
1	NGC 2543	8:12:56.2	36:14:42.7	39.13 ± 0.04	220 ± 20	6.4 ± 0.1	0.052 ± 0.007	<4.0		36.42	6.82
2	NGC 2543	8:12:57.2	36:14:48.6	39.07 ± 0.02	320 ± 10	6.59 ± 0.08	0.027 ± 0.002	<4.0		32.49	6.82
1	NGC 2748	9:13:32.6	76:27:55.0	39.33 ± 0.03	292 ± 7	6.66 ± 0.05	0.043 ± 0.002	11.0 ± 0.8	9.0 ± 2.0	9.14	7.09
2	NGC 2748	9:13:30.6	76:27:41.9	39.23 ± 0.03	270 ± 9	6.55 ± 0.07	0.043 ± 0.003	6.0 ± 0.7	3.0 ± 1.0	9.95	7.07
1	NGC 3041	9:53:2.4	16:39:41.7	39.02 ± 0.03	293 ± 7	6.5 ± 0.06	0.03 ± 0.002	4.5 ± 0.7	2.2 ± 0.8	22.31	6.93
2	NGC 3041	9:53:6.5	16:41:35.4	39.02 ± 0.02	381 ± 7	6.67 ± 0.03	0.0202 ± 0.0007	<4.0		1.4	7.25
1	NGC 2712	8:59:33.4	44:55:27.5	39.65 ± 0.04	230 ± 10	6.7 ± 0.1	0.09 ± 0.009	12.2 ± 0.8	9.0 ± 2.0	51.86	6.81
2	NGC 2712	8:59:32.7	44:55:14.4	39.21 ± 0.03	300 ± 8	6.61 ± 0.05	0.036 ± 0.002	11.9 ± 0.8	12.0 ± 3.0	38.87	6.82
1	NGC 5740	14:44:23.7	1:40:52.4	39.33 ± 0.02	185 ± 5	6.35 ± 0.05	0.086 ± 0.004	42.0 ± 2.0	170.0 ± 30.0	39.41	6.82
2	NGC 5740	14:44:25.3	1:40:51.6	39.18 ± 0.02	361 ± 9	6.72 ± 0.04	0.026 ± 0.001	5.6 ± 0.5	2.5 ± 0.6	15.91	6.92
1	NGC 6412	17:29:27.3	75:41:25.2	39.96 ± 0.03	404 ± 7	7.18 ± 0.04	0.055 ± 0.002	19.3 ± 0.7	12.0 ± 2.0	2.48	7.17
2	NGC 6412	17:29:27.4	75:41:25.4	39.33 ± 0.02	340 ± 10	6.75 ± 0.06	0.035 ± 0.002	6.4 ± 0.9	3.0 ± 1.0	2.39	7.17
1	NGC 6207	16:43:3.5	36:50:10.5	39.51 ± 0.03	154 ± 6	6.33 ± 0.07	0.14 ± 0.01	18.0 ± 1.0	27.0 ± 6.0	120.66	6.78
2	NGC 6207	16:43:3.8	36:50:3.4	39.36 ± 0.03	131 ± 4	6.15 ± 0.06	0.148 ± 0.009	13.9 ± 0.9	21.0 ± 5.0	0.51	7.38
1	NGC 1073	2:43:38.3	1:23:38.6	39.22 ± 0.03	124 ± 3	6.04 ± 0.05	0.138 ± 0.007	13.4 ± 0.5	23.0 ± 3.0	1868.64	6.39
2	NGC 1073	2:43:39.6	1:23:43.3	38.87 ± 0.06	87 ± 3	5.64 ± 0.08	0.16 ± 0.01	9.9 ± 0.6	23.0 ± 5.0	521.43	6.59
1	NGC 3423	10:51:19.2	5:51:8.5	39.64 ± 0.02	407 ± 5	7.03 ± 0.03	0.038 ± 0.001	14.5 ± 0.3	9.3 ± 0.8	17.46	6.95
2	NGC 3423	10:51:18.9	5:51:19.4	39.37 ± 0.02	236 ± 8	6.54 ± 0.06	0.063 ± 0.004	6.7 ± 0.6	<4.0 ± 1.0	16.14	6.9
1	NGC 428	1:12:53.2	0:56:47.5	39.27 ± 0.02	167 ± 2	6.26 ± 0.03	0.093 ± 0.003	10.8 ± 0.4	12.0 ± 1.0	28.12	6.83
2	NGC 428	1:12:53.2	0:56:47.5	39.03 ± 0.03	155 ± 4	6.09 ± 0.06	0.08 ± 0.005	5.7 ± 0.6	5.0 ± 1.0	28.22	6.83
1	NGC 5334	13:52:55.8	−1:5:18.9	38.93 ± 0.01	171 ± 6	6.11 ± 0.06	0.061 ± 0.004	<4.0		57.57	6.8
2	NGC 5334	13:52:52.3	−1:6:46.8	38.81 ± 0.02	172 ± 7	6.05 ± 0.07	0.053 ± 0.004	<4.0		29.0	6.83
1	NGC 5112	13:22:2.4	38:43:15.2	39.55 ± 0.04	288 ± 7	6.75 ± 0.06	0.057 ± 0.003	11.6 ± 0.5	8.0 ± 1.0	155.01	6.77
2	NGC 5112	13:22:2.0	38:43:15.0	39.54 ± 0.04	215 ± 6	6.56 ± 0.06	0.088 ± 0.005	12.4 ± 0.6	11.0 ± 2.0	137.97	6.78
1	NGC 3403	10:53:56.6	73:41:27.7	38.78 ± 0.05	200 ± 10	6.1 ± 0.1	0.041 ± 0.005	9.2 ± 0.8	15.0 ± 5.0	13.86	7.03
2	NGC 3403	10:53:58.5	73:41:19.6	38.71 ± 0.05	171 ± 9	6.0 ± 0.1	0.048 ± 0.005	4.2 ± 0.8	<4.0 ± 2.0	39.29	6.82
1	NGC 4639	12:42:55.5	13:14:53.2	38.63 ± 0.08	160 ± 9	5.9 ± 0.1	0.047 ± 0.006	10.8 ± 0.8	26.0 ± 8.0	50.94	6.81
2	NGC 4639	12:42:49.1	13:16:7.4	38.33 ± 0.03	238 ± 6	6.02 ± 0.05	0.0186 ± 0.0009	7.8 ± 0.9	16.0 ± 5.0	75.81	6.8
1	NGC 7241	22:15:49.3	19:13:49.7	38.64 ± 0.03	126 ± 5	5.76 ± 0.07	0.069 ± 0.005	<4.0		130.24	6.78
2	NGC 7241	22:15:49.7	19:13:48.1	38.54 ± 0.08	106 ± 5	5.6 ± 0.1	0.08 ± 0.008	8.0 ± 2.0	20.0 ± 10.0	94.91	6.79
2	NGC 918	2:25:49.6	18:30:25.2	38.58 ± 0.04	87 ± 3	5.49 ± 0.07	0.111 ± 0.007	10.2 ± 0.7	34.0 ± 8.0	52.28	6.81
1	NGC 4324	12:23:6.2	5:15:1.7	39.31 ± 0.02	165 ± 5	6.28 ± 0.05	0.1 ± 0.005	<4.0		5.74	7.1
2	NGC 4324	12:23:5.1	5:14:53.4	37.97 ± 0.06	84 ± 5	5.2 ± 0.1	0.058 ± 0.007	<4.0		10.56	7.06
1	NGC 4389	12:25:31.5	45:43:5.6	38.98 ± 0.02	161 ± 6	6.09 ± 0.07	0.071 ± 0.005	13.0 ± 1.0	25.0 ± 6.0	12.86	7.04
2	NGC 4389	12:25:31.4	45:43:5.1	38.59 ± 0.01	199 ± 9	6.03 ± 0.07	0.033 ± 0.002	4.6 ± 0.7	<4.0 ± 2.0	15.44	6.94
1	NGC 4498	12:31:39.5	16:51:22.2	38.7 ± 0.03	120 ± 3	5.76 ± 0.06	0.079 ± 0.005	13.3 ± 0.7	43.0 ± 8.0	30.39	6.83
2	NGC 4498	12:31:41.4	16:50:51.4	38.6 ± 0.06	80 ± 3	5.44 ± 0.09	0.13 ± 0.01	5.7 ± 0.6	11.0 ± 3.0	70.1	6.8
1	NGC 2541	8:14:40.4	49:2:30.7	39.48 ± 0.04	160 ± 3	6.34 ± 0.05	0.127 ± 0.006	18.4 ± 0.3	29.0 ± 3.0	44.26	6.81
2	NGC 2541	8:14:36.3	49:3:7.6	39.19 ± 0.03	119 ± 3	6.0 ± 0.06	0.143 ± 0.009	14.2 ± 0.5	28.0 ± 5.0	90.61	6.79
1	NGC 2500	8:1:46.9	50:44:3.3	38.44 ± 0.04	76 ± 4	5.3 ± 0.1	0.12 ± 0.01	7.7 ± 0.6	24.0 ± 7.0	214.74	6.76
2	NGC 2500	8:1:59.7	50:45:57.8	38.4 ± 0.04	99 ± 2	5.49 ± 0.05	0.075 ± 0.004	9.4 ± 0.8	33.0 ± 8.0	20.71	6.96

This paper has been typeset from a TEX/LATEX file prepared by the author.